UNIVERSITY OF ROCHESTER
LABORATORY FOR LASER ENERGETICS

Volume 80
July–September 1999
DOE/SF/19460-321

LLE Review

Quarterly Report

About the Cover:

Both the cover photo and the photograph to the left show Research Associate Leon Waxer operating an LLE-designed IR streak camera. This camera was used extensively for collecting data required to activate the new 2-D SSD system reported on in this LLE Review. The flexibility of this instrument along with a built-in control system allowed for rapid configuration changes from acquiring data in the SSD driver area (single beam at 64-mm diameter) to beamline output measurements. Dr. Waxer is shown measuring the amplitude modulation induced by SSD near the output of the OMEGA beamlines where the aperture is 200 mm in diameter and the camera must be operated with multiple input slit orientations.

The work described in this volume includes current research at the Laboratory for Laser Energetics, which is supported by New York State Energy Research and Development Authority, the University of Rochester, the U.S. Department of Energy Office of Inertial Confinement Fusion under Cooperative Agreement No. DE-FC03-92SF19460, and other agencies.

Printed in the United States of America
Available from
National Technical Information Services
U.S. Department of Commerce
5285 Port Royal Road
Springfield, VA 22161
Price codes: Printed Copy A03
Microfiche A01

For questions or comments, contact Samuel F. B. Morse, *Editor*, Laboratory for Laser Energetics, 250 East River Road, Rochester, NY 14623-1299, (716) 275-9672; e-mail: smor@lle.rochester.edu

Worldwide-Web Home Page: http://www.lle.rochester.edu/

UNIVERSITY OF ROCHESTER
LABORATORY FOR LASER ENERGETICS

Volume 80
July–September 1999
DOE/SF/19460-321

LLE Review

Quarterly Report

UR LLE

Contents

In Brief

This volume of the LLE Review, covering the period July–September 1999, features a theoretical analysis of a process that generates mass perturbations of an imploding target driven by modulated laser illumination. The process, referred to as "laser imprint," impacts the integrity of the shell during direct-drive implosions, potentially quenching target performance. In this article V. N. Goncharov, J. A. Delettrez, S. Skupsky, and R. P. J. Town present a model of the generation of mass perturbations and analyze the mass perturbation growth due to nonuniform ablation pressure. Stabilizing mechanisms of thermal conduction smoothing and mass ablation are shown to suppress the acceleration perturbation, and mass ablation is also shown to impact velocity perturbations. The model predicts that a direct-drive cryogenic NIF target will remain intact during the implosion when 1-Thz SSD beam smoothing is used.

Additional highlights of the research presented in this issue are

- R. W. Short describes modeling of the stability of self-focused filaments in laser-produced plasmas. Wave-equation treatment of the laser light combined with self-consistent filament equilibrium simulations indicates that only very small filaments, where one waveguide mode is propagating, may be considered to be stable. When two or more waveguide modes can propagate, the filament tends to break up within tens of microns.

- J. D. Zuegel, D. Jacobs-Perkins, J. A. Marozas, R. G. Roides, W. Bittle, E. M. R. Michaels, R. S. Craxton, J. H. Kelly, T. J. Kessler, W. Seka, and S. Skupsky present the implementation of broadband smoothing on OMEGA with two-dimensional smoothing by spectral dispersion. This article describes issues relevant to the architecture choices made during the design phase of the project, as well as measurements conducted to verify the laser bandwidth and ensure that FM to AM conversion is minimized.

- T. R. Boehly, V. N. Goncharov, O. Gotchev, J. P. Knauer, D. D. Meyerhofer, D. Oron, S. P. Regan, Y. Srebro, W. Seka, D. Shvarts, S. Skupsky, and V. A. Smalyuk discuss the effect of temporal pulse shape on laser imprint and beam smoothing. Preimposed modulations on planar-foil targets were used to calibrate the mass equivalence of features imprinted by the laser, and resulting growth rates are comparable to numerical simulations.

- A. Babushkin, M. J. Harvey, and M. D. Skeldon present a model for the output signal-to-noise ratio (SNR) of a regenerative amplifier (regen). Noise from a regen oscillator comes from amplified spontaneous emission and SNR of the injected pulse. Experimental results presented are in excellent agreement with theory.

- S. Arrasmith and S. D. Jacobs discuss the development of new magnetorheological fluids (MRF) used to extend the finishing technique to two soft, single-crystal, optical materials: CaF_2 and KDP. Material removal functions are characterized through analysis of polishing spots generated on a new research platform at the Center for Optics Manufacturing.

- This volume concludes with the 1999 Summer High School Program Report, the FY99 Laser Facility Report, and the National Laser Users' Facility News.

Samuel F. B. Morse
Editor

Modeling Laser Imprint for Inertial Confinement Fusion Targets

In inertial confinement fusion (ICF), a spherical shell filled with a DT-gas mixture is compressed to high densities and temperatures to achieve ignition condition.[1] Degradation from spherical symmetry during the implosion, however, limits the achievable compression ratios and could quench the ignition. The main source of such asymmetry is hydrodynamic instabilities (such as the Rayleigh–Taylor and Bell–Plesset instabilities) seeded by both irradiation nonuniformities and impurities in the target materials. In this article we describe a process that generates mass perturbations on an initially uniform target driven by a modulated laser illumination. Such a process is referred to as a "laser imprint." The control of laser imprint is of crucial importance for the successful implosion of direct-drive ICF targets. To evaluate the imprint growth, the following two physical problems must be considered: (1) generation of nonuniformities in ablation pressure due to spatial modulations in a laser intensity, and (2) mass perturbation growth on a target driven by nonuniform ablation pressure. A detailed analysis of the first problem can be found in Refs. 2. The second problem, however, has not been adequately treated in the past. In Ref. 3, for example, perturbation growth was derived by using the Chapman–Jouguet deflagration model. As discussed in Refs. 4, such a model neglects thermal smoothing of perturbations in the conduction zone (a region between the critical surface and ablation front), and in addition, it does not reproduce the main restoring force, which is due to a difference in the dynamic pressure at the peaks and valleys of the front distortion.[5,6] An improved model has been proposed in Ref. 4, where thermal smoothing of the pressure perturbations has been included. At the ablation front, however, the authors used the "Landau–Darrieus" boundary condition that, similar to the result of Ref. 3, neglects the main stabilizing force due to the dynamic overpressure.

The main goal of this article is to give a theoretical description of the hydrodynamic coupling between the pressure perturbation and the ablation-front modulation. The developed theory is relevant to the stability of high-isentrope ($\alpha \geq 2$, where α is the ratio of the pressure at a given density to the Fermi pressure) ICF targets directly driven by a laser pulse that consists of a low-intensity (a few 10^{13} W/cm^2) foot followed by the main drive pulse. During the foot pulse, the ablation pressure created by the mass ablation generates a shock wave that propagates through the shell. Since the laser intensity is constant during the shock transit time, the pressure behind the shock is uniform and the ablation front travels at a constant velocity. Later, as intensity increases during the main pulse (in direct-drive cryogenic target designs the beginning of the main pulse is timed to the first shock breakout of the shell[7]), the shell starts to accelerate and front perturbations η begin to grow because of Rayleigh–Taylor (RT) instability $\eta \sim \eta_0 e^{\gamma_{\mathrm{RT}} t}$, where γ_{RT} is the RT instability growth rate. If the perturbation amplitude becomes too large during the implosion, the shell breaks up, and the ignition condition cannot be reached. To quantify the shell integrity, we introduce an "integrity factor" $\Upsilon = A_{\mathrm{mix}}/\Delta R$, which is defined as a ratio of the mix amplitude (bubble amplitude) A_{mix} to the shell thickness ΔR. The bubble amplitude is taken to be[1] $A_{\mathrm{mix}} = \sqrt{2}\sigma$, where

$$\sigma^2 = \sum_{l,m} \left|\eta_{l,m}(t)\right|^2 \Big/ (4\pi)$$

is the rms sum of the modes, $\eta_{l,m} = \int d\Omega Y^*_{l,m}(\Omega)\, R(\Omega,t)$, $R(\Omega,t)$ is the radius at solid angle Ω and time t, and $Y^*_{l,m}$ is the complex conjugate of the l,m spherical harmonic. The shell remains intact during the implosion if the integrity factor is less than unity ($\Upsilon < 1$ for all time). Simulations performed for direct-drive cryogenic OMEGA and NIF target designs show that to satisfy the condition $\Upsilon < 1$ during the implosion, the integrity factor Υ_0 at the shock breakout time t_{br} must be less than $\Upsilon_0^{\mathrm{max}} = 0.01$. In this article we present a model to estimate $\Upsilon_0^{\mathrm{imp}}$ due to the laser imprint. Such a model sheds some light on physical mechanisms driving the laser-imprint growth. To proceed with our analysis, first we note that during the prepulse, the shell's outer radius R is much larger than the target thickness ΔR, and convergence effects can be neglected. All perturbations are then decomposed in the Fourier space $\eta = \sum_k \eta_k e^{ikx}$, where

$$\eta_k \simeq \eta_{l,m}\sqrt{\frac{(2l+1)}{8\pi}},$$

$k \simeq l/R$ is the wave number, and l is mode number. Since the perturbation amplitude in the linear regime is proportional to the laser nonuniformity, we introduce a normalized amplitude $\eta_{k,\delta I} \equiv \eta_k/(\delta I_k/I_0)$, where δI_k is the Fourier component of the intensity modulation and I_0 is the average intensity. Then, the integrity factor takes the following form:

$$\Upsilon^2 \equiv \Sigma_k\, \Upsilon_k^2 = \Sigma_k \left|\eta_{k,\delta I}(\delta I_k/I_0)/\Delta R\right|^2.$$

Nonuniformity in the laser illumination $\delta I_k/I_0$ can be obtained from the spectrum of the laser speckle on target produced by the distributed phase plates (DPP's). Thus, to estimate the integrity factor, we must calculate an imprint amplitude $\eta_{\rm imp} \equiv \eta_{k,\delta I}/\Delta R$ at the shock breakout time (beginning of the main pulse) $t = t_{\rm br} = \Delta R_0/U_s$, where ΔR_0 is the uncompressed shell thickness and U_s is the shock speed. For strong shocks [when the ratio of the ablation pressure p_a and the initial pressure of the undriven shell p_0 is large $(\Pi \equiv p_a/p_0 >> 1)$] and the ratio of specific heat $\gamma = 5/3$, the shock breakout time is $t_{\rm br} \simeq 2\Delta R/c_s$, where c_s is sound speed of compressed material and $\Delta R \simeq \Delta R_0/4$.

The laser imprint growth is determined by several physical effects. First, as the laser energy is absorbed by the outmost layer of the shell at the beginning of implosion, the shell material heats up, launching a heat wave toward the pellet center. Material behind the heat front expands outward, creating an ablation pressure p_a that induces a shock wave propagating through the shell. Nonuniformities in the intensity across the laser beam cause different parts of the beam to ablate shell material at different rates, generating an ablation-pressure modulation $\tilde{p}_a$ along the ablation front. Since the shock speed U_s scales as a square root of the shock strength Π ($U_s \sim \sqrt{\Pi}$ for $\Pi >> 1$), stronger shocks launched at the peaks of ablation pressure propagate faster than the shocks launched at the pressure valleys. A difference in the shock speed distorts the shock front and creates a perturbed velocity field inside the compressed region. A velocity perturbation at the ablation front, in turn, leads to a linear-in-time front distortion growth $\eta \sim \tilde{v}_x t$, where $\tilde{v}_x \sim \tilde{p}_a U_s/(2p_a)$, and the x axis points in the direction of laser propagation. Note that such a growth is wavelength independent. Then, in order to conserve the tangential component of the fluid velocity, a rippled shock front generates a lateral mass flow from the convex part of the shock front (which protrudes the most into the cold region) into the concave part (Fig. 80.1). A change in density, according to the adiabatic condition $\partial_t \tilde{p} = c_s^2 \partial_t \tilde{\rho}$, leads to a pressure deficiency in the convex part and a pressure excess in the concave part. Since the pressure perturbation at the ablation front is fixed by the laser-beam nonuniformities, the lateral flow creates a negative pressure gradient toward the convex part of the shock front and a positive one toward the concave part. The pressure gradient accelerates fluid elements $\rho d_t^2 \eta = \rho \tilde{a} \sim \partial_x \tilde{p}_a$, leading to an additional perturbation growth $\eta \sim \partial_x \tilde{p}_a/(2\rho)t^2$, where ρ is the compressed density and η is the ablation front amplitude. After the shock front has moved a distance of the order of perturbation wavelength from the ablation front, the latter reaches a steady state (assuming that the ablation pressure modulation is constant in time), and the pressure perturbation in the vicinity of the ablation front obeys Laplace's equation $\partial_x^2 \tilde{p} - k^2 \tilde{p} = 0$. Keeping only a decaying solution of that equation, $\tilde{p} \sim \tilde{p}_a e^{-kx}$, leads to a finite pressure gradient, a perturbed acceleration of the ablation front, $\tilde{a} \sim \partial_x \tilde{p}_a/\rho \simeq k\tilde{p}_a/\rho$, and a quadratic-in-time asymptotic perturbation growth $\eta(kc_s t >> 1) \sim (\tilde{p}_a/\rho)kt^2/2$.

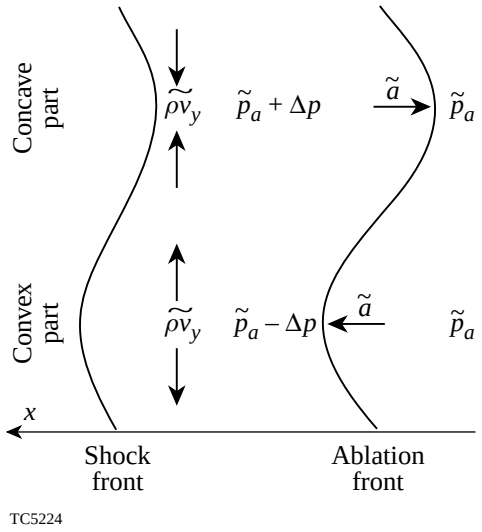

Figure 80.1
Lateral mass flow generated by the rippled shock creates a pressure excess behind the concave part of the shock front and a pressure deficiency behind the convex part.

A rigorous derivation of the perturbation evolution in the "classical" case (constant-in-time ablation-pressure modulation and no mass ablation) is performed by solving the mass, momentum, and energy conservation equations. Such a derivation (to be discussed in detail in a forthcoming paper[8]) yields a result similar to the one obtained above by using a simple physical argument. For strong shocks $\Pi >> 1$ and $\gamma = 5/3$, the

solution is

$$\eta(t) \simeq \frac{\tilde{p}_a}{p_a}\left(0.7\, c_s t + 0.3\, k c_s^2 t^2\right). \quad (1)$$

Note that Eq. (1) can be reproduced by solving a simple second-order differential equation

$$d_t^2 \eta = \tilde{a} = k\frac{\tilde{p}_a}{\gamma p_a} c_s^2 \quad (2)$$

with the initial conditions $\eta(0) = 0$ and $\eta'(0) = 0.7\left(\tilde{p}_a / p_a\right) c_s$. To calculate the imprint amplitude η_{imp}, we assume[2] $p_a \sim I^{2/3}$ and $\delta I_k / I_0 = (3/2)\tilde{p}_a / p_a$, hence

$$\eta_{\text{imp}}^{\text{cl}} \simeq 0.8\, k\Delta R + 0.9 \simeq 0.8\frac{l}{A} + 0.9, \quad (3)$$

where $A = R/\Delta R$ is the shell's in-flight aspect ratio (IFAR). Equation (3) shows that the imprint amplitude of long-wavelength modes ($k\Delta R << 1$ or $l < 15$ for directly driven NIF targets) is wavelength independent; at short wavelengths, however, the imprint amplitude is proportional to the mode number l and inversely proportional to the IFAR. In addition, the imprint amplitude in the classical case does not depend on the laser intensity. Next, we calculate the integrity factor for a direct-drive $\alpha = 3$ NIF target design[7] using η_{imp} in the form of Eq. (3). The amplitudes $\delta I_k / I_0$ can be estimated by using the results of Ref. 9. The calculation yields $\Upsilon_0^{\text{imp}} \simeq 0.2$, which is a factor of 20 larger than the stability threshold $\Upsilon_0^{\max}$. The RT instability seeded by such a perturbation would disrupt the shell during the acceleration phase of implosion and quench the ignition. In direct-drive ICF, however, several physical processes significantly reduce the imprint growth. Next, we consider the main stabilizing mechanisms inherent to laser-driven targets: thermal conduction smoothing and mass ablation.

Thermal Conduction Smoothing

As the heat front (ablation front) propagates into the cold portion of the target, material heats up and expands outward creating a hot plasma corona. The laser light is absorbed in a region (absorption region) where the density of blown-off material is much lower than the compressed shell density. Thus, a finite zone (conduction zone) of hot plasma exists between where the laser energy is deposited and the ablation front. Because of the high temperatures, any pressure perturbations inside such a region are smoothed out by the thermal conduction. The simplest theory[10] predicts that pressure perturbations decay exponentially away from the critical surface ("cloudy-day effect") $\tilde{p} \sim e^{-kx}$; thus, nonuniformities in the ablation pressure are reduced by a factor e^{-kD_c}, where D_c is a distance between the absorption region and the ablation front. More-sophisticated models of thermal smoothing[2] yield similar behavior of the reduction coefficient. To simplify the analysis, the distance D_c is taken to be $D_c \simeq V_c t$; this leads to an exponential decay in the ablation pressure perturbation $\tilde{p}_a \simeq \tilde{p}_a(0) e^{-kV_c t}$. After $t = \left(kV_c\right)^{-1}$, laser nonuniformities with the wave number k decouple from the ablation front, nullifying the k-Fourier component of the perturbed acceleration $\tilde{a}$. The ripple of the ablation front, however, continues to grow due to a finite velocity perturbation

$$\eta\left[t > \left(kV_c\right)^{-1}\right] \sim \tilde{v}_x t.$$

Scaling laws of the perturbation growth can be derived by solving Eq. (2) and substituting $\tilde{p}_a = \tilde{p}_a(0) e^{-kV_c t}$ into its right-hand side:

$$d_t^2 \eta_a = k\frac{\tilde{p}_a(0)}{\gamma p_a} c_s^2 e^{-kV_c t}. \quad (4)$$

The imprint amplitude in this case takes the following form:

$$\eta_{\text{imp}}^{\text{th}} \simeq \frac{0.4\, A}{l}\left(\frac{c_s}{V_c}\right)^2 \left(e^{-\Delta_c} - 1\right) + 0.9 + 0.8\frac{c_s}{V_c}, \quad (5)$$

where $\Delta_c = 2(l/A)V_c/c_s$. Equation (5) shows that for modes with $\Delta_c > 1$ ($l > 10$ for direct-drive NIF targets) thermal smoothing reduces the imprint amplitude by a factor $\eta_{\text{imp}}^{\text{th}} / \eta_{\text{imp}}^{\text{cl}} \sim A/l$.

Mass Ablation

An additional reduction in the imprint growth is due to the mass ablation. The main stabilizing mechanism produced by ablation is the dynamic overpressure or "rocket effect"[5,6] that can be described as follows: Laser-beam nonuniformities create ablation-pressure modulations along the target surface. Such modulations (see discussion earlier in the text) distort the ablation front: front peaks protrude into the hot plasma corona, and the valleys move toward the cold target material. Analysis of Ref. 5 shows that because of high thermal conductivity in the blowoff region, temperature is uniform along the heat (ablation) front. Thus the ablation front's distortion growth slightly increases the temperature gradient at the front peaks and decreases it at the front valleys. An increase in the temperature gradient leads to an additional heat flow that speeds up the

heat front and increases the velocity of the blown-off material $V_{\rm bl}$. Higher blowoff ("exhaust") velocity creates an excess in the dynamic pressure ("rocket effect" increases). At the perturbation valleys, the picture is reversed: a reduction in the temperature gradient decreases the ablation and blowoff velocities, thus the dynamic pressure and the rocket effect are also reduced. We can conclude that the modulation in the dynamic pressure created by the thermal conduction reduces the perturbation growth and ultimately stabilizes the growth completely. Calculations[5] show that the amplitude of the dynamic pressure is proportional to the front distortion $\tilde{p}_d = \dot{m} V_{\rm bl} k\eta$. Hence, perturbations reach a saturation value $\eta_{\rm sat}$ when the dynamic-pressure modulation balances the ablation-pressure modulation $\tilde{p}_a \sim \dot{m} V_{\rm bl} k\eta_{\rm sat}$, where $\dot{m} = \rho V$ is the mass ablation rate. Next, to perform a quantitative stability analysis, we solve the system of conservation equations assuming a sharp interface at the ablation front and a constant-in-time ablation-pressure modulation $\tilde{p}_a$.[8] Skipping lengthy calculations, we report a final formula for the asymptotic behavior ($kc_s t >> 1$) of the front-surface perturbations in the case of strong shocks $\Pi >> 1$ and $\gamma = 5/3$:

$$\frac{\eta(t)}{\tilde{p}_a/(\gamma p_a)} \simeq \frac{kc_s^2}{\omega^2}(1 - D\cos\omega t) + \frac{c_s}{\omega}\left(1.2 - \frac{2c_s}{V_{\rm bl}}\right) D\sin\omega t + \eta_v(t), \qquad (6)$$

where $D = e^{-2kV_a t}$, V_a and $V_{\rm bl}$ are the ablation and blowoff velocities, respectively, and $\omega = k\sqrt{V_a V_{\rm bl}}$. The last term η_v is due to the vorticity convection from the shock toward the ablation front:

$$\eta_v = \frac{2c_s}{kV_{\rm bl}}\left[e^{kV_a t}\int_{kV_a t}^{\infty} e^{-\tau}\Omega(2\tau)d\tau - 1.2\ D\cos\omega t\right],$$

where

$$\Omega = i(\nabla \times \mathbf{v})_z \big/ (kc_s \tilde{p}_a/\gamma p_a) \simeq 3J_0(\tau) - 2J_4(\tau)$$

is the normalized vorticity and $J_n(\tau)$ is the Bessel function. Equation (6) shows that the front perturbation grows according to Eq. (1) until the distortion amplitude becomes big enough and the dynamic overpressure balances the ablation-pressure perturbation. After that time, the ablation front oscillates around an average amplitude $<\eta> = \eta_{\rm sat}$. In addition, the difference in the ablation velocity at the distortion peaks and valleys and also the vorticity convection from the ablation front damp the perturbation amplitude [factor $e^{-2kV_a t}$ in Eq. (6)].

The next step is to combine effects of the mass ablation and thermal smoothing. An analytical solution of conservation equations in this case has a very lengthy form.[8] We omit a rigorous derivation of such a solution in this article, however, noting that the essential physics of the imprint growth reduction can be described by an approximate solution derived from Eq. (2) with the following modifications: To take into account the mass ablation effects, first, we add to the left-hand side of Eq. (2) the stabilizing term due to the dynamic overpressure (rocket effect) $\omega^2\eta$, and then, the damping term $4kV_a d_t\eta$, which is due to the difference in the mass ablation rate at the front peaks and valleys and also to the vorticity convection downstream from the ablation front. Thermal smoothing of the pressure perturbations inside the conduction zone is included, the same way as in Eq. (4), by introducing a reduction factor $e^{-kV_c t}$ into the right-hand side of Eq. (2). As a result, the equation describing the evolution of the ablation-front distortion takes the following form:

$$d_t^2\eta + 4kV_a d_t\eta + \omega^2\eta = k\frac{\tilde{p}_a(0)}{\gamma p_a}c_s^2 e^{-kV_c t}. \qquad (7)$$

Observe that neglecting the reduction factor $e^{-kV_c t}$ yields solution (6) (except for the vorticity term η_v). Substituting the solution of Eq. (7) into the definition of the imprint amplitude gives

$$\eta_{\rm imp}^{\rm abl} \simeq 0.4\frac{A}{l}\hat{\eta}\left(e^{-\Delta_c} - e^{-2\Delta_a}\cos\Delta_{\rm bl}\right) + \frac{e^{-2\Delta_a}}{\Delta_{\rm bl}}\left(0.9 + 0.8\frac{V_c}{c_s}\hat{\eta}\right)\sin\Delta_{\rm bl} + \eta_v^{\rm imp}, \qquad (8)$$

where

$$\hat{\eta} = c_s^2/\left(V_a V_{\rm bl} + V_c^2\right),$$

$$\Delta_a = 2(l/A)V_a/c_s,$$

$$\Delta_{\rm bl} = 2(l/A)\sqrt{V_a V_{\rm bl}}/c_s,$$

and

$$\eta_v^{\text{imp}} = 0.8\left(A/l\right)\left(c_s/V_{\text{bl}}\right)e^{\Delta_a}$$

$$\times\int_{\Delta_a}^{\infty} e^{-\tau}\Omega(2\tau)\,d\tau - 1.2e^{-2\Delta_a}\cos\Delta_{\text{bl}}.$$

Equation (8) shows that in the presence of the mass ablation, the imprint amplitude has an oscillatory dependence on the mode number. For modes with $\Delta_a < 1$, the oscillation period and amplitude are determined by the velocity and acceleration perturbation growth reduced by the dynamic overpressure and the mass ablation [the first two terms in Eq. (8)]. For modes with $\Delta_a > 1$, the acceleration and velocity perturbations deposited at the ablation front are damped by the mass ablation [factor e^{-2kV_at} in Eq. (6)], and the behavior of such modes are determined by the vorticity convection from the shock front [the last term in Eq. (8)]. Figure 80.2 shows a comparison of the imprint amplitude calculated for conditions specified in Ref. 7 with and without stabilizing effects. Observe a significant reduction in the imprint growth due to the thermal smoothing and the mass ablation. To apply Eq. (8) to the ICF target designs, the blowoff velocity is taken to be[6,11]

$$V_{\text{bl}} = V_a\Big/\left[\mu(v)\left(kL_0\right)^{1/v}\right],$$

where v is the power index for thermal conduction, L_0 is the characteristic thickness of the ablation front,

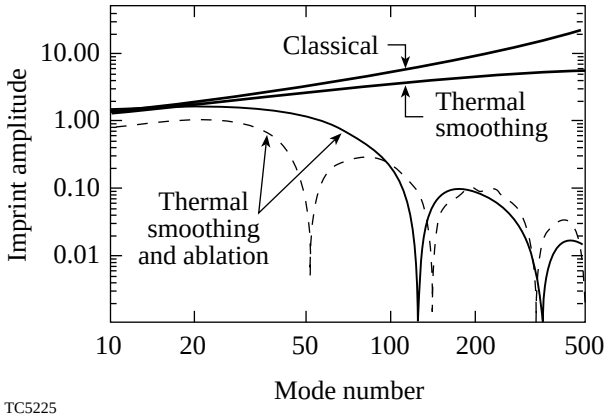

Figure 80.2
Plot of imprint amplitude versus mode number calculated using Eqs. (3), (5), and (8) (solid lines) and 2-D *ORCHID* simulation (dashed line) for a direct-drive, "all-DT," $\alpha = 3$, NIF target design.

$$\mu = \left(2/v\right)^{1/v}\Big/\Gamma\left(1+1/v\right) + 0.12/v^2,$$

and $\Gamma(x)$ is the gamma function. The parameters L_0 and v are obtained by using the fitting procedure described in Ref. 11. For a direct-drive, "all-DT," $\alpha = 3$, NIF cryogenic target design,[7] the 1-D numerical simulations and the fitting procedure give $V_a = 2.5\ \mu$m/ns, $V_c \simeq 30\ \mu$m/ns, $c_s \simeq 37\ \mu$m/ns, $L_0 \simeq 0.03\ \mu$m, and $v \simeq 2$. The imprint efficiency calculated by using Eqs. (3), (5), and (8) is plotted in Fig. 80.2 (solid line). For comparison, the results of the 2-D *ORCHID*[12] simulations of single-wavelength imprint amplitudes (dashed line) are shown on the same plot with the model prediction. Observe that the developed model accurately reproduces the oscillatory behavior of the imprint growth. Next, using Eq. (8), the integrity factor is calculated to be $\Upsilon_0^{\text{imp}} = 1.2\times10^{-2}$. Since the outer-surface roughness and also the perturbation "feedout" from the inner surface[13] make an additional contribution to the rms nonuniformity, the total integrity factor is expected to exceed the stability threshold $\Upsilon_0^{\max}$, thus an additional reduction in the imprint amplitude is required for a successful implosion. A significant improvement in beam uniformity has been made in recent years by introducing SSD[14] (smoothing by spectral dispersion) and ISI[15] (induced spatial incoherence) smoothing techniques. To include the effect of SSD in our simulations, the intensity nonuniformities have been reduced by factor

$$\sqrt{t_c/\left(t_c + 4t\right)}$$

that gives on average a reduction in rms nonuniformity

$$\sigma = \sqrt{t_c/t_{\text{avg}}}\,\sigma_0,$$

where the coherence time is taken to be[14]

$$t_c = \left[\Delta v \sin\left(k\delta/2\right)\right]^{-1},$$

Δv is the bandwidth, t_{avg} is the averaging time, and δ is the speckle size. Simulations show that using the 2-D SSD smoothing technique with 1-THz laser bandwidth reduces the integrity factor to $\Upsilon_0^{\text{imp}} = 10^{-3}$, which is a factor of 10 lower than the threshold Υ_0.

In summary, a model describing the evolution of the laser imprint was developed. The model shows that the imprint growth is determined by the velocity and acceleration pertur-

bations generated by the laser-beam nonuniformities. Thermal smoothing inside a hot plasma corona suppresses only the acceleration perturbation, while the mass ablation suppresses both velocity and acceleration perturbations. The model predicts that a direct-drive cryogenic NIF target will remain intact during the implosion when the laser is smoothed with 1-THz SSD used in current direct-drive target designs.

ACKNOWLEDGMENT

This work was supported by the U.S. Department of Energy Office of Inertial Confinement Fusion under Cooperative Agreement No. DE-FC03-92SF19460, the University of Rochester, and the New York State Energy Research and Development Authority. The support of DOE does not constitute an endorsement by DOE of the views expressed in this article.

REFERENCES

1. J. D. Lindl, *Inertial Confinement Fusion: The Quest for Ignition and Energy Gain Using Indirect Drive* (Springer-Verlag, New York, 1998).

2. J. Sanz *et al.*, Phys. Fluids **31**, 2320 (1988); W. M. Manheimer, D. G. Colombant, and J. H. Gardner, Phys. Fluids **25**, 1644 (1982).

3. R. Ishizaki and K. Nishihara, Phys. Rev. Lett. **78**, 1920 (1997).

4. R. J. Taylor *et al.*, Phys. Rev. Lett. **79**, 1861 (1997); A. L. Velikovich *et al.*, Phys. Plasmas **5**, 1491 (1998).

5. J. Sanz, Phys. Rev. E **53**, 4026 (1996); V. N. Goncharov, R. Betti, R. L. McCrory, P. Sorotokin, and C. P. Verdon, Phys. Plasmas **3**, 1402 (1996); A. R. Piriz, J. Sanz, and L. F. Ibanez, Phys. Plasmas **4**, 1117 (1997).

6. V. N. Goncharov, Phys. Rev. Lett. **82**, 2091 (1999).

7. S. V. Weber, S. G. Glendinning, D. H. Kalantar, M. H. Key, B. A. Remington, J. E. Rothenberg, E. Wolfrum, C. P. Verdon, and J. P. Knauer, Phys. Plasmas **4**, 1978 (1997); R. P. J. Town, F. J. Marshall, J. A. Delettrez, R. Epstein, P. W. McKenty, D. D. Meyerhofer, P. B. Radha, S. Skupsky, and C. Stoeckl, Bull. Am. Phys. Soc. **43**, 1666 (1998).

8. V. N. Goncharov, R. Betti, J. A. Delettrez, P. W. McKenty, S. Skupsky, and R. P. J. Town, "Stability Analysis of Directly Driven OMEGA and NIF Targets," to be submitted to Physics of Plasmas.

9. R. Epstein, J. Appl. Phys. **82**, 2123 (1997).

10. K. A. Brueckner and S. Jorna, Rev. Mod. Phys. **46**, 325 (1974); S. E. Bodner, J. Fusion Energy **1**, 221 (1981).

11. R. Betti, V. N. Goncharov, R. L. McCrory, and C. P. Verdon, Phys. Plasmas **5**, 1446 (1998).

12. R. L. McCrory and C. P. Verdon, in *Computer Applications in Plasma Science and Engineering*, edited by A. T. Drobot (Springer-Verlag, New York, 1991).

13. R. Betti, V. Lobatchev, and R. L. McCrory, Phys. Rev. Lett. **81**, 5560 (1998).

14. S. Skupsky, R. W. Short, T. Kessler, R. S. Craxton, S. Letzring, and J. M. Soures, J. Appl. Phys. **66**, 3456 (1989); S. Skupsky and R. S. Craxton, Phys. Plasmas **6**, 2157 (1999).

15. R. H. Lehmberg, A. J. Schmitt, and S. E. Bodner, J. Appl. Phys. **62**, 2680 (1987).

Stability of Self-Focused Filaments in Laser-Produced Plasmas

The filamentation instability causes local intensity maxima in a laser beam propagating through a plasma to self-focus to high intensities. This process can affect many aspects of the beam propagation and absorption, so it has long been a subject of interest in laser–plasma interaction research. The theoretical thresholds and growth rates for the linear phase of the filamentation instability are readily determined analytically.[1] As the instability develops beyond the linear phase and the filament becomes smaller and more intense, the self-focusing effect is counterbalanced by diffraction. This leads to the possibility of a nonlinear inhomogeneous equilibrium—a steady-state, high-intensity, low-density filament in which the plasma pressure outside is balanced by the ponderomotive force of the light inside. This nonlinear phase of the instability, which produces the highest intensities and is therefore of the greatest practical interest, is difficult to treat analytically because of the strong density and intensity inhomogeneities associated with such a filament. The nonlinear stage of filamentation is usually studied using simulation codes that directly integrate the equations of motion for the fields and particles or fluids.[2] One important problem that is difficult to study in this way, however, concerns the long-term stability of the nonlinearly saturated filament, once formed. A stable filament would have a greater influence on absorption nonuniformity and on beam bending[3]—important considerations for direct- and indirect-drive laser-fusion schemes, respectively. It would also be expected to make a greater contribution to parametric instabilities.[4–6] An investigation of the stability of a filament through simulation would require the simulation to cover a large spatial extent of plasma over a long period of time. At present, due to computational limitations,[7] such extensive simulations necessitate some approximations in the equations used to describe the filament, in particular the paraxial approximation to the wave equation for the light propagation. This approximation requires that the propagating light not develop wave-vector components that deviate far from the initial direction of the beam. Recent studies[8] indicate, however, that the filaments most likely to be stable are very intense and have very small radii, of the order of the light wavelength, so that the paraxial approximation is questionable. Moreover, a simulation can treat only one specific set of irradiation and plasma parameters at a time, and extrapolating from simulations based on a limited sampling of parameter space to general results on stability is problematic.

A purely analytic approach to filament stability requires many approximations and idealizations to render the problem at all tractable; for this reason applying the few results that have been obtained analytically to realistic filaments is difficult. These results do suggest, however, that filaments may be unstable to kinking or bending perturbations[9] and to necking or "sausage" perturbations,[10] with the latter having a faster growth rate.

In this article the stability problem of a realistic filament will be addressed for the first time using a semi-analytic approach. A dispersion relation is obtained that describes the linear growth of a sausage-type perturbation of a self-consistent, self-focused cylindrical filament in equilibrium. This dispersion relation is analogous to the simple polynomial dispersion relations obtained for the instabilities of a plane electromagnetic wave in a homogeneous plasma.[11] Rather than being a polynomial in the perturbation wave number and frequency as in the homogeneous case, however, the filament dispersion relation depends on these quantities through ordinary differential equations that must be solved numerically for each value of the frequency and wave number. This is still much easier than the simultaneous solution of several coupled partial differential equations as required by a simulation, yet it allows the consideration of a physically realistic filament equilibrium, arbitrarily long space and time intervals, and the use of the full wave equation to describe the light propagation.

We will show that filament stability depends crucially on filament size. First, consider the case where the filament is small enough that only one waveguide mode will propagate. The pump (laser) light propagates through the filament in this fundamental mode at frequency ω_0 and axial wave number k_0. Amplitude modulation (sausaging) results from adding a perturbing light wave in the same mode at a differing frequency

$\omega_0 + \Delta\omega$ and wave number $k_0 + \Delta k$, $\Delta\omega$ and Δk being related by the dispersion relation for the waveguide mode. This intensity modulation itself has frequency $\Delta\omega$ and wave number Δk and tends to move along the filament at the waveguide group velocity $\Delta\omega/\Delta k$, which in general is comparable to the speed of light. Because the speed of the perturbation greatly exceeds the ion-sound speed, the perturbation interacts weakly with the surrounding plasma, limiting potential growth rates. A much stronger interaction can be expected if the filament is large enough to allow two or more waveguide modes to propagate. In this case the perturbing light can be in a second mode with a different dispersion relation. Thus, it can have a frequency $\omega_1 \cong \omega_0$ but a significantly smaller axial wave number $k_1 < k_0$, so that $\Delta\omega/\Delta k = (\omega_0 - \omega_1)/(k_0 - k_1)$ is much smaller than the speed of light and can be comparable to the ion-sound speed, leading to an enhanced interaction.

To explore these ideas quantitatively, we consider an equilibrium filament consisting of a low-density cylindrical channel in a higher-density homogeneous background plasma. The channel is formed by the ponderomotive pressure of light propagating within the channel in the fundamental waveguide mode. Assume that in equilibrium the axis of the filament lies in the z direction and the filament intensity and density vary only as a function of r. Write the electric field E_0 of the pump wave as

$$\frac{e}{v_T m\omega_0} E_0(r,z,t) = \psi_0(r) e^{i(k_0 z - \omega_0 t)} + \text{c.c.}, \qquad (1)$$

so that ψ_0 represents the oscillatory velocity $v_0 = eE_{\max}/m\omega_0$ normalized to v_T, the electron thermal velocity. The pump satisfies the wave equation in cylindrical geometry

$$\left[c^2\left(\frac{d^2}{dr^2} + \frac{1}{r}\frac{d}{dr}\right) + \omega_0^2 - \omega_{p0}^2(r) - c^2k_0^2\right]\psi_0(r) = 0, \qquad (2)$$

with boundary conditions $\psi_0(r) \to 0$ as $r \to \infty$, $(d\psi_0/dr)_{r=0} = 0$ for a bound-state waveguide mode propagating in a cylindrical filament. The square of the plasma frequency $\omega_{p0}^2(r)$ is proportional to the density, which is determined by pressure balance with the ponderomotive force of the pump:

$$\frac{\omega_{p0}^2(r)}{\omega_0^2} = \frac{n_0(r)}{n_c} = \frac{N_0}{n_c} e^{-\frac{1}{4}\psi_0^2(r)}, \qquad (3)$$

where N_0 is the background density outside the filament and n_c is the critical density. Equations (2) and (3) give a nonlinear differential equation for ψ_0, which together with the boundary conditions results in an eigenvalue problem determining k_0, ψ_0, and the filament density profile $n_0(r)$. The pump propagates in the fundamental mode; however, if the filament is deep and wide enough, higher-order waveguide modes will also propagate in it. These eigenmodes satisfy the equation

$$\left[\frac{d^2}{ds^2} + \frac{1}{s}\frac{d}{ds} - \frac{n_0(s)}{n_c}\right]\phi_j(s) = \Gamma_j\phi_j(s), \qquad (4)$$

where $j = 0$ represents the fundamental mode, $s \equiv \omega_0 r/c$, and the eigenvalue Γ_j determines the relation between the axial wave number k_j of the eigenmode and its frequency ω_j: $c^2k_j^2/\omega_0^2 - \omega_j^2/\omega_0^2 = \Gamma_j$. In general, the spectrum of eigenvalues Γ_j will contain discrete values for bound modes with $\Gamma_j - N_0/n_c$ and a continuum of unbound modes with $\Gamma_j - N_0/n_c$. Since we are interested in instability, we will be primarily concerned with the bound modes; the unbound modes propagate away from the filament before they have an opportunity to grow significantly. The eigenfunctions are orthogonal and assumed normalized to unity. The pump is assumed proportional to the fundamental eigenmode: $\psi_0(s) = \alpha_0\phi_0(s)$, where α_0 may be taken real and represents the pump amplitude.

We employ fluid equations for the plasma density; linearizing n around the equilibrium density profile $n_0(r)$ results in an inhomogeneous driven wave equation for the density perturbation $n_1(r,z,t)$:

$$\frac{\partial^2 n_1}{\partial t^2} - c_s^2\left\{\nabla^2 n_1 - \frac{\nabla n_0}{n_0}\cdot\nabla n_1 + \left[\frac{(\nabla n_0)^2}{n_0^2} - \frac{\nabla^2 n_0}{n_0}\right]n_1\right\}$$

$$= -\frac{Z}{M}\left[n_0\nabla\cdot\mathbf{F}_p + (\nabla n_0)\cdot\mathbf{F}_p\right], \qquad (5)$$

where c_s is the ion acoustic speed, Z and M are the ion charge and mass, respectively, and $\mathbf{F}_p$ is the ponderomotive force resulting from the electromagnetic waves.

The density perturbation n_1 is assumed to have real wave number k in the z direction (along the filament) and frequency ω, which may be complex: $n_1(r,z,t) = n(r)e^{i(kz-\omega t)} + \text{c.c.}$ The interaction of the density perturbation with the pump generates a perturbed electromagnetic wave:

$$\psi_1(r,z,t) = \left\{\psi_+(r)e^{i\left[(k+k_0)z-(\omega+\omega_0)t\right]} + \psi_-(r)e^{i\left[(k-k_0)z-(\omega-\omega_0)t\right]}\right\} + \text{c.c.},$$

where, since the frequency ω may be much smaller than ω_0, both upshifted and downshifted terms are kept. The linearized wave equation then becomes

$$\left[\frac{d^2}{ds^2}+\frac{1}{s}\frac{d}{ds}+\left(1\pm\frac{c_s}{c}\Omega\right)^2-\left(\kappa_0\pm\kappa\right)^2-\frac{n_0(s)}{n_c}\right]\psi_\pm(s) = \frac{n(s)}{n_c}\psi_0(s). \tag{6}$$

The first-order ponderomotive force resulting from the beating of the pump and perturbed electromagnetic waves is

$$\begin{aligned}\mathbf{F}_p &= -mv_T^2\nabla\left(\psi^2\right)_1 \\ &= -mv_T^2\nabla\left\{\left[\psi_0^*(s)\psi_+(s)+\psi_0(s)\psi_-(s)\right]\times e^{i(\kappa\zeta-\Omega\tau)}+\text{c.c.}\right\}.\end{aligned} \tag{7}$$

In Eqs. (6) and (7) we have introduced the dimensionless quantities $\Omega = \omega c/\omega_0 c_s$, $\kappa = \omega_0 k/c$, $\varsigma = \omega_0 z/c$, and $\tau = c_s\omega_0 t/c$. Substituting Eq. (7) into Eq. (5), we obtain an equation for the perturbed density in terms of the perturbed electromagnetic fields:

$$\begin{aligned}&\left[\frac{d^2}{ds^2}+\left(\frac{1}{s}-\frac{1}{n_0}\frac{dn_0}{ds}\right)+\Omega^2-\kappa^2+\frac{1}{n_0^2}\left(\frac{dn_0}{ds}\right)^2 - \frac{1}{n_0}\frac{d^2n_0}{ds^2}-\frac{1}{n_0}\frac{1}{s}\frac{dn_0}{ds}\right]\frac{n(s)}{n_c} \\ &= -\frac{n_0(s)}{n_c}\left[\frac{d^2}{ds^2}+\left(\frac{1}{s}+\frac{1}{n_0}\frac{dn_0}{ds}\frac{d}{ds}\right)-\kappa^2\right] \times\left(\psi_0\psi_+ + \psi_0\psi_-\right).\end{aligned} \tag{8}$$

It is useful to expand the electromagnetic fields in terms of the orthonormal eigenfunctions $\phi_j(s)$ of Eq. (4):

$$\psi_\pm(s) = \sum_{j=1}^{\infty}\beta_j^\pm\phi_j(s).$$

Defining $\eta_j(s)$ as the solution of

$$\begin{aligned}&\left[\frac{d^2}{ds^2}+\left(\frac{1}{s}-\frac{1}{n_0}\frac{dn_0}{ds}\right)\frac{d}{ds}+\Omega^2-\kappa^2+\frac{1}{n_0^2}\left(\frac{dn_0}{ds}\right)^2 - \frac{1}{n_0}\frac{d^2n_0}{ds^2}-\frac{1}{n_0}\frac{1}{s}\frac{dn_0}{ds}\right]\eta_j(s) \\ &= -\frac{n_0(s)}{n_c}\left[\frac{d^2}{ds^2}+\left(\frac{1}{s}+\frac{1}{n_0}\frac{dn_0}{ds}\right)\frac{d}{ds}-\kappa^2\right]\phi_0(s)\phi_j(s),\end{aligned} \tag{9}$$

satisfying the boundary conditions $\eta_j'(0) = 0$ and outgoing waves as $s\to\infty$, we see from Eq. (8) that the density perturbation can be written as

$$\frac{n(s)}{n_c} = \alpha_0\sum_j\left(\beta_j^+ + \beta_j^-\right)\eta_j(s). \tag{10}$$

Combining Eqs. (6) and (10) then gives a linear relation among the coefficients $\beta_j^\pm$:

$$\begin{aligned}&\left[\left(1\pm\frac{c_s}{c}\Omega\right)^2-1-\left(\kappa_0\pm\kappa\right)^2+\Gamma_j\right]\beta_j^\pm \\ &= \alpha_0^2\sum_{j'}\left(\beta_{j'}^\pm+\beta_{j'}^\mp\right)L_{jj'},\end{aligned} \tag{11}$$

where the $L_{jj'}$ denote the integrals over the wave functions: $L_{jj'} = \int_0^\infty\phi_j(s)\eta_{j'}(s)\phi_0(s)sds$.

While the sums in Eq. (11) extend over an infinite range of j, only the finite number of discrete bound states are of interest in studying instabilities, and in small filaments only a few of these may exist. Truncating the sums in Eq. (11) to the bound states leads to a finite set of linear homogeneous equations in the $\beta_j^\pm$, and setting the determinant of the coefficients to zero

gives a dispersion relation relating Ω and κ. Unlike the homogeneous case, however, this dispersion relation is not a polynomial but a more complicated function of Ω and κ, since the coefficients $L_{jj'}$ depend on Ω and κ through the solutions of the differential equation (9). These solutions are readily obtained numerically, however, allowing the evaluation of the dispersion relation and the determination of the unstable modes of the filament and their growth rates.

As an example, consider a background plasma with a uniform density of half-critical, $N_0/n_c = 0.5$, and an ion sound speed of $c_s = 10^{-3}\,c$, corresponding to an electron temperature of approximately 1 keV. For a given central field amplitude $\psi_0(0)$, the filament density and intensity profiles are found by integrating Eqs. (2) and (3), adjusting the axial wave number k_0 so that the boundary conditions are satisfied. The waveguide modes are then found from Eq. (4). At this density and temperature a central intensity of $\psi_0(0) \equiv v_0/v_T = 7$ is found to be sufficient to produce a filament wide enough to allow two electromagnetic modes to propagate. The resulting pump field amplitude and filament density profile are shown in Fig. 80.3(a), and the two normalized waveguide modes are shown in Fig. 80.3(b).

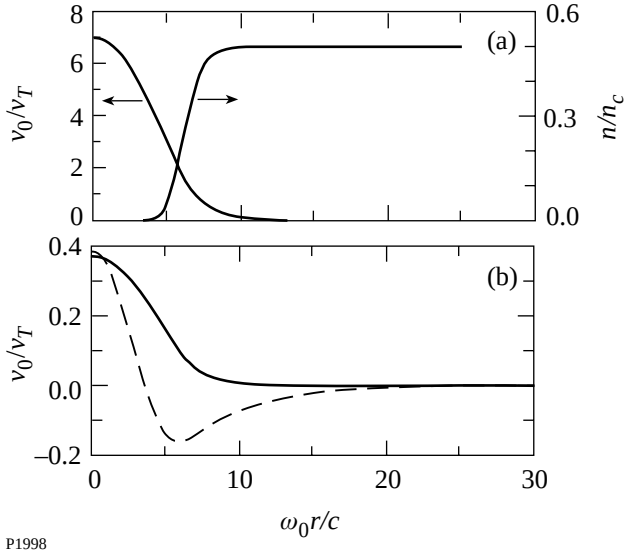

Figure 80.3
(a) Self-consistent equilibrium field and density profiles for a filament with background plasma density $n_0/n_c = 0.5$ and central intensity $v_0/v_T = 7$; (b) the two normalized bound eigenmodes for this filament.

The temporal growth rates and real frequencies for perturbations having the form of the fundamental eigenmode are shown in Figs. 80.4(a) and 80.4(b), plotted against the normalized axial wave number κ. The group velocity of the perturbation normalized to the sound speed can be obtained from the slope of the real frequency curve in Fig. 80.4(b) and, as expected, is near the speed of light: $v_g/c_s \cong 900$ (recall $c/c_s = 1000$ in this example). Thus, a perturbation will propagate along the filament at nearly the speed of light as it grows, leading to a spatial growth rate that can be estimated by dividing the temporal growth rates in Fig. 80.3(a) by $v_g/c_s \cong 900$. This spatial growth rate is quite small, of order $10^{-4}\,\omega_0/c$. For a typical laser-fusion experiment wavelength of 0.351 μm, for example, a small perturbation to a filament could propagate for several thousand microns before becoming large enough to disrupt the filament. Laser-produced plasmas of interest are generally much smaller than this, so that small filaments (radius < one wavelength) are effectively stable to perturbations of this form.

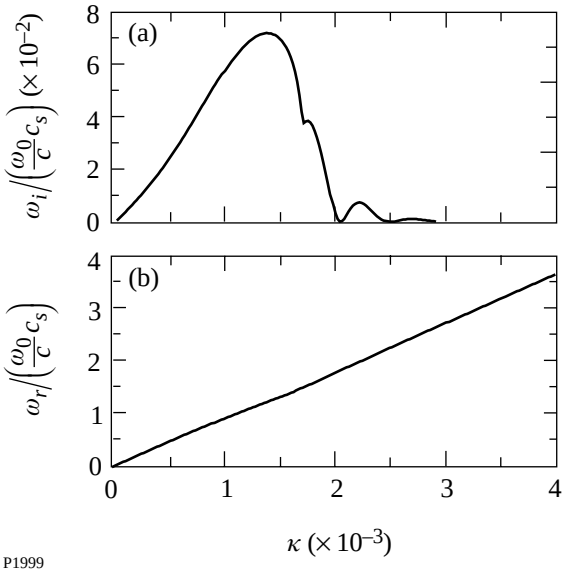

Figure 80.4
Growth rates (a) and real frequencies (b) for perturbations in the form of the fundamental eigenmode (solid line) in Fig. 80.3(b).

The situation is more interesting for filaments large enough that two or more waveguide modes will propagate. Figures 80.5(a) and 80.5(b) show the temporal growth rate and real frequency for the perturbation corresponding to the second waveguide mode for the same filament parameters as in Fig. 80.4. Note that the growth rate is now considerably larger, but more significant is the fact that the axial wave number of the perturbation (given by the difference in the two waveguide-mode wave numbers) is much larger than in the single-mode case. This makes the group velocity [Fig. 80.5(c)] at which the perturbation propagates much smaller, and the resulting

spatial growth rate much larger. This effect is due to the fact that having two different dispersion relations for the interacting modes allows larger values of Δk for a given $\Delta\omega$. More importantly, however, the fact that the group velocity in Fig. 80.5(c) passes through zero suggests the possibility of an absolute instability, which grows without propagation. If we define κ_{max} to be the value of κ for which the temporal growth rate in Fig. 80.5(a) is a maximum, and Ω_{max}, Ω'_{max}, Ω''_{max} to be the corresponding frequency and its first and second derivatives with respect to κ, the condition for absolute instability is[12]

$$\mathrm{Im}(\Omega_{max}) > \frac{1}{2}(\Omega'_{max})^2\,\mathrm{Im}\left(\frac{1}{\Omega''_{max}}\right).$$

Evaluation of these quantities shows that this condition is well satisfied (the left side in this example is 0.164, and the right is 0.047), so that the instability is indeed absolute. This means that the perturbation will remain in place as it grows, rather than propagating along the filament. Unless saturated by some nonlinear mechanism, such an instability would be expected to quickly disrupt the filament.

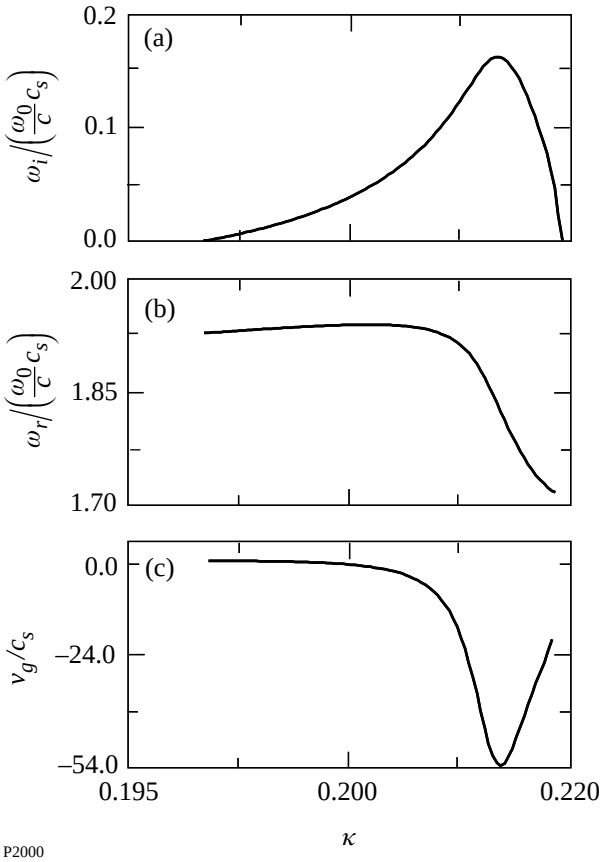

Figure 80.5
Growth rates (a), real frequencies (b), and group velocities (c) for perturbations in the form of the second eigenmode (dashed line) in Fig. 80.3(b).

When the filament is large enough that many modes will propagate, one approaches a "classical" regime where the propagating light may be treated by the paraxial approximation or ray tracing. From the above analysis it is expected that such filaments would be unstable, which seems to be the case in simulations.[7,8]

The above stability analysis has been concerned with a sausage-type perturbation, i.e., one with no azimuthal variation in the cylindrical coordinates centered on the equilibrium filament. "Kink-type" modes, with nonvanishing azimuthal wave numbers, could be treated using a straightforward extension of the above analysis. Such modes would, of course, require a filament large enough to carry these higher-order modes, so small single-mode filaments would be unaffected. Larger filaments could be unstable to both kink and sausage perturbations; which one dominates in practice is a subject for further research. Another topic requiring further study is the effect of plasma inhomogeneity, though by analogy with other wave–plasma interactions, inhomogeneity might be expected to reduce instability growth rates.

In conclusion, the first analysis of filament stability using a realistic self-consistent filament equilibrium and a wave-equation treatment of light propagation has been carried out using a semi-analytic approach. It is found that small filaments that carry light in only one waveguide mode have only a weak convective instability and, in most cases of interest in laser–plasma interactions, may be regarded as essentially stable. Filaments large enough to carry two or more waveguide modes are unstable to sausage-type perturbations, which can be absolutely unstable and may lead in typical cases to distortion or breakup of the filament within a few tens of microns.

ACKNOWLEDGMENT

This work was supported by the U.S. Department of Energy Office of Inertial Confinement Fusion under Cooperative Agreement No. DE-FC03-92SF19460, the University of Rochester, and the New York State Energy Research and Development Authority. The support of DOE does not constitute an endorsement by DOE of the views expressed in this article.

REFERENCES

1. P. Kaw, G. Schmidt, and T. Wilcox, Phys. Fluids **16**, 1522 (1973).

2. D. E. Hinkel *et al.*, Phys. Plasmas **5**, 1887 (1998).

3. D. E. Hinkel, E. A. Williams, and C. H. Still, Phys. Rev. Lett. **77**, 1298 (1996).

4. T. Afshar-rad *et al.*, Phys. Fluids B **4**, 1301 (1992).

5. R. W. Short, W. Seka, and R. Bahr, Phys. Fluids **30**, 3245 (1987).

6. R. W. Short and A. Simon, Phys. Plasmas **5**, 4134 (1998).

7. A. J. Schmitt and B. B. Afeyan, Phys. Plasmas **5**, 503 (1998).

8. F. Vidal and T. W. Johnston, Phys. Rev. Lett. **77**, 1282 (1996).

9. E. Valeo, Phys. Fluids **17**, 1391 (1974).

10. E. J. Valeo and K. G. Estabrook, Phys. Rev. Lett. **34**, 1008 (1975).

11. W. L. Kruer, *The Physics of Laser–Plasma Interactions*, Frontiers in Physics, Vol. 73, edited by D. Pines (Addison-Wesley, Redwood City, CA, 1988).

12. L. S. Hall and W. Heckrotte, Phys. Rev. **166**, 120 (1968).

Broadband Beam Smoothing on OMEGA with Two-Dimensional Smoothing by Spectral Dispersion

High laser-irradiation uniformity is an important requirement for successful implosions of inertial confinement fusion (ICF) targets,[1] particularly for the direct-drive OMEGA laser system that directly illuminates ICF targets. Direct-drive laser irradiation that is not perfectly uniform imprints on the target surface and perturbs the spherical symmetry. This seeds the Rayleigh–Taylor hydrodynamic instability during the target acceleration phase and can severely degrade target performance. Target imprinting is determined when the critical surface decouples from the ablation surface. The critical surface corresponds to the highest density reached by the plasma, where the laser frequency equals the plasma frequency. The ablation surface corresponds roughly to the surface separating the inward-flowing (imploding) plasma and the outward-flowing "exhaust." Direct-drive smoothing techniques must minimize the level of irradiation nonuniformity on a time scale comparable to or shorter than this imprinting phase. Initial target experiments indicate that this imprinting phase lasts for several hundred picoseconds on OMEGA and depends on the spatial wavelength of the most important perturbations.

Direct-drive laser irradiation uniformity for different ranges of spatial frequencies is achieved on OMEGA by a number of techniques.[1] The number of beams, as well as power and energy balance among beams, predominantly affects irradiation nonuniformity at low spatial frequencies, while higher spatial frequencies are determined by the individual beam uniformity achievable with smoothing by spectral dispersion (SSD).

The technique of SSD significantly reduces irradiation nonuniformity by rapidly shifting the laser speckle pattern generated on the target by distributed phase plates (DPP's).[2] A high-frequency electro-optic phase modulator produces a time-varying wavelength modulation that is angularly dispersed by a diffraction grating. Significant smoothing is achieved on a time scale approximately equal to the inverse bandwidth impressed by the phase modulator. Two-dimensional SSD (2-D SSD) extends the smoothing benefits of SSD by combining the deflections of the laser speckle pattern on target in two orthogonal directions. Two separate stages of bulk electro-optic phase modulators and gratings are employed that generate and disperse bandwidth in two orthogonal directions.

Broadband Two-Dimensional SSD Generation

The principal relationships governing irradiation uniformity with SSD are illustrated in Fig. 80.6(a), which plots the rms irradiation nonuniformity for all spatial frequencies (for modes with $\ell \leq 500$) on target for several different SSD configurations versus integrating time. The initial smoothing rate is directly proportional to the SSD bandwidth since the coherence time for the speckle pattern produced by the DPP is inversely related to the effective bandwidth in any time slice of the pulse. The asymptotic nonuniformity is inversely related to the square root of the number of independent speckle patterns on the target. For an SSD system employing critical dispersion, this corresponds to the number of FM sidebands imposed on the beam by the phase modulator.

Incorporating a higher-frequency phase modulator in the 2-D SSD system offers two different approaches to improving irradiation uniformity on OMEGA: increasing the total SSD bandwidth or producing multiple SSD color cycles.

1. Large SSD bandwidths can be generated for a given number of critically dispersed FM sidebands and propagated through the laser system since less grating dispersion is required to achieve a single color cycle. Increased SSD bandwidths smooth laser irradiation faster. An asymmetric 2-D SSD configuration on OMEGA using phase modulators operating at 3.3 and 10.4 GHz can produce infrared bandwidths of 1.5×11 Å at nominally 1×1 color cycles, respectively. This infrared bandwidth corresponds to a UV bandwidth of approximately 1 THz.

2. Multiple SSD color cycles can be produced with a higher modulation frequency using the current grating design without exceeding the beam divergence limit imposed by the laser system pinholes. Increasing the number of color cycles accelerates the smoothing at the mid-range spatial frequencies (ℓ = 50–200) that pose the greatest threat of

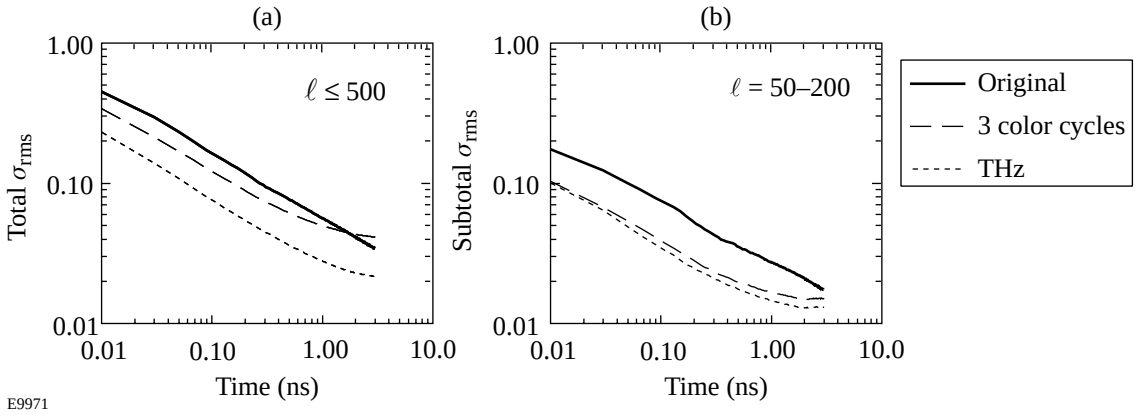

Figure 80.6
The intial rate of SSD smoothing is governed by the total bandwidth, while the asymptotic nonuniformity is related to the total number of independent speckle patterns on target. If at least one SSD color cycle is present, this corresponds to the number of FM sidebands produced by the phase modulators. (a) Plotting total nonuniformity ($\ell \leq 500$) versus averaging time shows that comparable smoothing levels should be achieved approximately four times sooner with the 1-THz SSD (1.5 × 11 Å, 1 × 1 color cycles) system than the original 2-D SSD (1.25 × 1.75 Å, 1 × 1 color cycles) system implemented on OMEGA, while the three-color-cycle 2-D SSD (1.5 × 3 Å, 1 × 3 color cycles) system actually achieves worse asymptotic levels since fewer independent speckles modes are produced. (b) Smoothing performance for the spatial frequencies associated with ℓ-modes in the range between 50 and 200 shows different behavior. The three-color-cycle SSD system performance during the first stage of smoothing is comparable to the 1-THz SSD system since the multiple color cycles preferentially smooth these spatial frequencies.

seeding hydrodynamic instabilities in direct-drive implosions. The current OMEGA FCC configuration can efficiently convert infrared bandwidths of 1.5 × 3.0 Å from modulators operating at 3.3 and 10.4 GHz to generate 1 × 3 color cycles, respectively.

The single-beam smoothing performance for several 2-D SSD implementations on OMEGA is compared in Fig. 80.6. Total rms nonuniformity is plotted versus integration time in Fig. 80.6(a). The original 2-D SSD implementation on OMEGA delivered approximately 0.2 THz of total SSD bandwidth in the ultraviolet (1.25 × 1.75 Å IR, 1 × 1 color cycles). Asymptotic nonuniformity levels of better than 2% are achieved after approximately 250 ps when multiple-beam overlap is included. In comparison, the 1-THz system (1.5 × 11 Å, 1 × 1 color cycles) planned for installation in November 1999 achieves improved asymptotic uniformity since it produces a larger number of independent speckle patterns and larger beam deflections. Furthermore, the integration time required to achieve 2% nonuniformity is reduced to about 70 ps.

The total smoothing performance of the three-color-cycle 2-D SSD system recently installed on OMEGA (1.5 × 3.0 Å, 1 × 3 color cycles) is also shown in Fig. 80.6(a). Poorer asymptotic performance is expected than for either of the other two systems since fewer independent speckle patterns are produced. Figure 80.6(b) presents the rms nonuniformity for the mid-range spatial frequencies versus integration time for the same 2-D SSD systems shown in Fig. 80.6(a). For these spatial frequencies, it can be seen that the smoothing performance of the three-color-cycle system is comparable to the 1-THz system. Direct comparisons of the target performance with both of these improved 2-D SSD systems will be performed once the 1-THz system is implemented.

For OMEGA, it is advantageous to implement the larger bandwidth and beam divergence in the second direction of the 2-D SSD setup since the bandwidth from the second modulator is not dispersed until after the most-limiting spatial-filter pinhole located in the large-aperture ring amplifier (LARA)[3] in the driver line. This constraint results from spatial-filtering requirements associated with the serrated aperture apodizer used to set the OMEGA beam profile. A slotted LARA spatial-filter pinhole with its long axis aligned along the direction of dispersed bandwidth is employed to maximize spatial filtering of the beam.

Larger spatial-filter pinholes are another important requirement for propagating broadband 2-D SSD on OMEGA. Pinhole sizes for the spatial filters in each of the six stages of OMEGA were originally chosen such that computed instantaneous intensities on the edge of any pinhole did not exceed 100 GW/cm^2[4] for a non-SSD, 1-ns FWHM Gaussian pulse. To perform this computation, a complete diffraction and non-

linear propagation model of the system was constructed. Amplitude noise, using the data of Stowers and Patton,[5,6] was applied to optical surfaces and the resulting pinhole irradiance calculated. For pinholes early in the system where spatial noise and its nonlinear growth were not an issue, the pinhole sizes were set no lower than approximately 13 times diffraction-limited in order to facilitate fabrication and alignment. Later optical time-domain reflectometry (OTDR) measurements on OMEGA indicated that in the beamline stages, the pinhole sizes were close to optimum for non-SSD high-energy shots. These same pinholes were operated with 1.25×1.75-Å bandwidth SSD with no deleterious effect or resultant amplitude modulation. Spatial noise measurements were also performed on OMEGA using a high-dynamic-range, far-field diagnostic, as shown in Fig. 80.7. The nonlinear growth of this noise was analyzed to establish the largest acceptable pinholes.

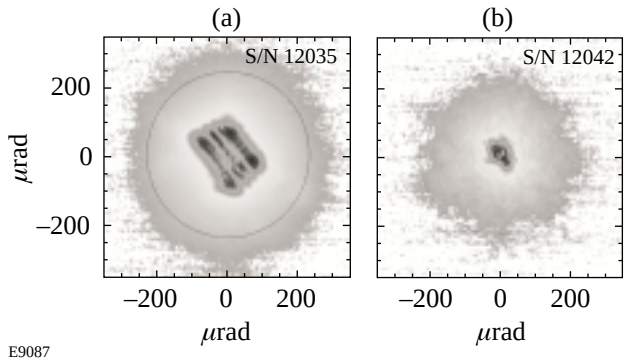

Figure 80.7
OMEGA spatial noise measurements and growth analysis set how much pinholes could be enlarged to accommodate broadband 2-D SSD.

For the current 1.5×3.0-Å SSD bandwidths, the pinholes were increased in diameter by the increase in the major dimension of the far-field spot (~50%). Since increased pinhole size increased the risk of system damage due to ripple growth[7] and Narcissus[8] (pencil beam) spots, a single beamline (40) of OMEGA was operated with these larger pinholes for a full year prior to their installation in the remainder of the system. No damage was observed in any of the optics in that beamline, which was exercised over the full range of OMEGA output energy and pulse shapes.

The 2-D SSD architecture implementing double-pass phase modulators and gratings shown in Fig. 80.8 was chosen for several reasons. Double-pass operation of a phase modulator increases its effective modulation efficiency, provided proper phase matching of the second pass is maintained. As a result, significantly lower microwave powers are required to achieve a given bandwidth while reducing the risk of air breakdown from the microwave fields in the microwave modulator resonators. Multiple-pass modulator operation can further increase the modulation efficiency but at the expense of increased system complexity.

Including a double-pass grating in the first SSD dimension also significantly reduces the space envelope required. Combining the first dimension predelay (G1) and dispersion (G2) functions into a single grating requires a far-field retroreflection to accomplish an image inversion; otherwise, the second pass through the grating would produce additional pulse distortion.

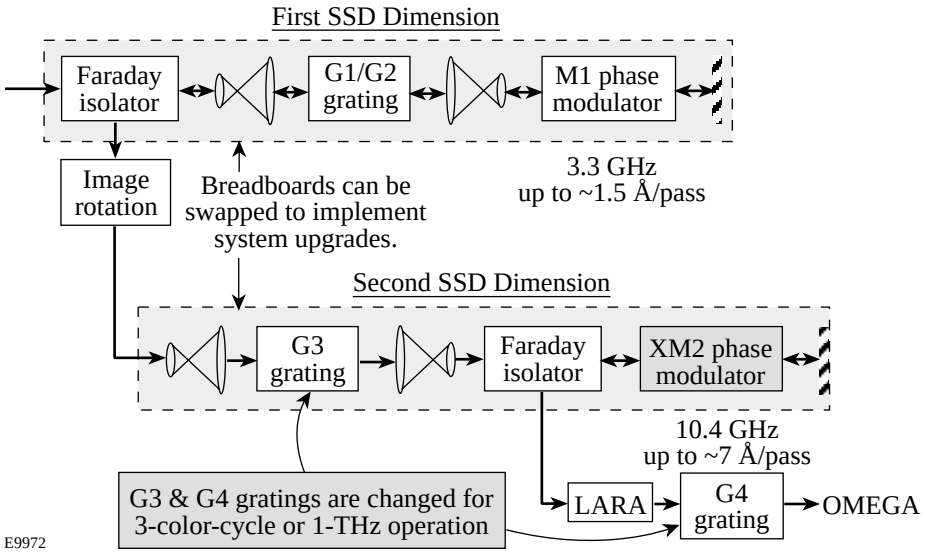

Figure 80.8
A double-pass, 2-D SSD architecture increases phase-modulator efficiency and reduces the space envelope required for a 2-D SSD system.

The two most important aspects of system performance for the improved 2-D SSD systems developed for OMEGA are bandwidth and FM-to-AM conversion. The 2-D SSD system is utilized as a "two-dimensional spectrometer" to measure the SSD bandwidths generated by each modulator, while an infrared streak camera system was developed to identify, measure, and minimize FM-to-AM conversion in the 2-D SSD system, as detailed below.

Accurate SSD bandwidth measurements for both phase modulators can be obtained simultaneously by capturing a far-field image of an SSD beam, as shown in Fig. 80.9, since the bandwidth generated by each phase modulator is dispersed in essentially orthogonal directions. Corrections for inexact dispersion matching between gratings G3 and G4, as well as imprecise image rotation between SSD directions, are accounted for using image-unwarping algorithms. The phase-modulation depth produced by each modulator is then determined by identifying the value for which a simulated spectrum best reproduces the measured spectral lineouts in each SSD direction, including the instrument's point spread function. For the three-color-cycle 2-D SSD system, FM spectra produced by the 10.4-GHz modulator are self-calibrating since the individual FM sidebands are completely resolved and the modulation frequency is accurately known.

Measuring the FM-to-AM conversion performance of the 2-D SSD systems is difficult, particularly for the 10.4-GHz modulation, since an instrument with sufficient bandwidth to measure the microwave modulation frequency and its harmonics is required. Additionally, the ability to verify performance across the beam profile is also important since some FM-to-AM conversion mechanisms manifest themselves in local variations. These requirements, plus the low repetition rate of our SSD pulses (5 Hz), eliminate sampling techniques and make an infrared streak camera the best instrument. The

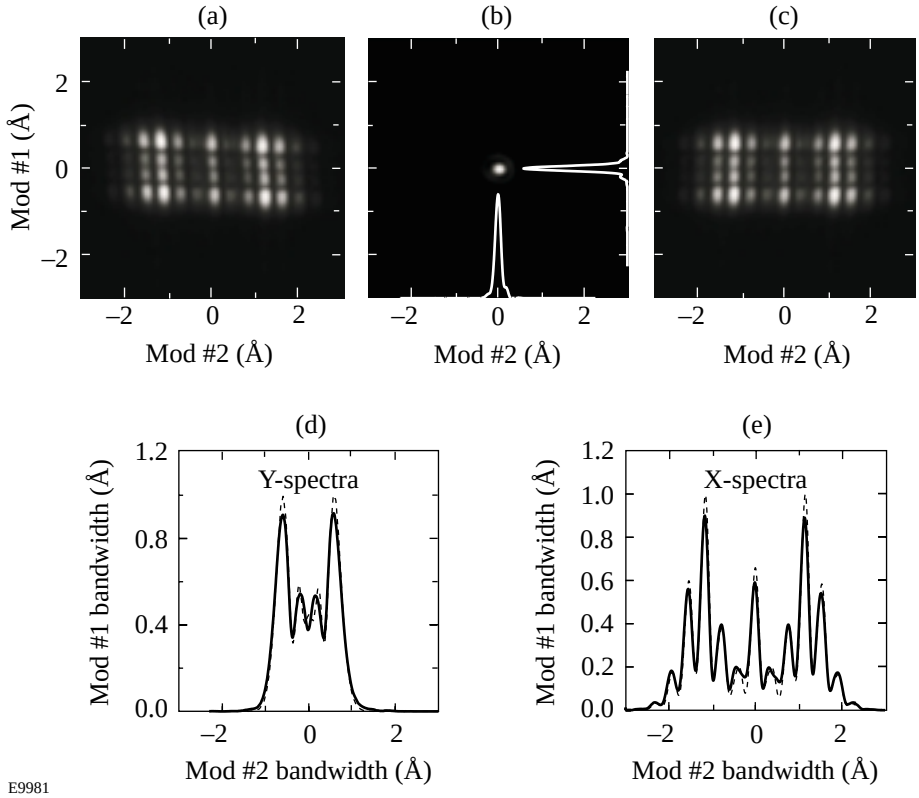

Figure 80.9
Far-field images of the 2-D SSD can be evaluated to measure FM bandwidth produced by each SSD modulator. (a) A raw image is captured on a scientific CCD. (b) The image for an unmodulated pulse is also captured to establish the instrumental response. (c) The image is corrected to account for image rotation errors introduced by the 2-D SSD system. In the corrected image, the bandwidth produced by each modulator is dispersed in orthogonal directions. (d) and (e) The bandwidth produced by each modulator is estimated by finding the simulated spectra (dashed), including the instrumental response, that best fit the measured spectra (solid).

uncoated photocathode of the streak camera is index matched to a wedged, AR-coated window to eliminate spurious etalon effects that would otherwise introduce amplitude modulation artifacts. Streak camera flat-field and time-base corrections are applied to account for instrumental nonlinearities.

FM-to-AM conversion in the 2-D SSD system is discriminated from modulation in the shaped-pulse input by transmitting a reference signal sampled before the 2-D SSD system to the streak camera using an optical fiber, as shown in Fig. 80.10(a). Lineouts at different spatial locations of the streak image [Fig. 80.10(b)] are normalized to this reference signal and the amplitude modulation estimated by finding the peak-to-valley variations of the ratio of these signals [Fig. 80.10(c)]. The signal-to-noise ratio of this measurement depends on the number of pixel rows averaged to produce the lineouts and appears to be limited by photon statistics. The harmonic content of the AM is easily obtained by fast Fourier transforming the difference of the signal and reference lineouts, as shown in Fig. 80.10(d). Statistically analyzing multiple streak images provides estimates of the uncertainty of these measurements.

FM-to-AM conversion in the 2-D SSD system was minimized by adjusting various system parameters and parametrically plotting the measured amplitude modulation to identify the optimal settings. For example, it is well known that propagation from an image plane of an SSD grating results in amplitude modulation. Amplitude modulation is minimized at an image plane of a grating that disperses SSD bandwidth. If an SSD grating is not properly located at the image plane of earlier gratings, the phase relationships between FM sidebands are disturbed and irreversibly convert FM to AM. SSD grating imaging was accomplished by plotting the measured AM as a function of image relay position, as shown in Fig. 80.11(a).

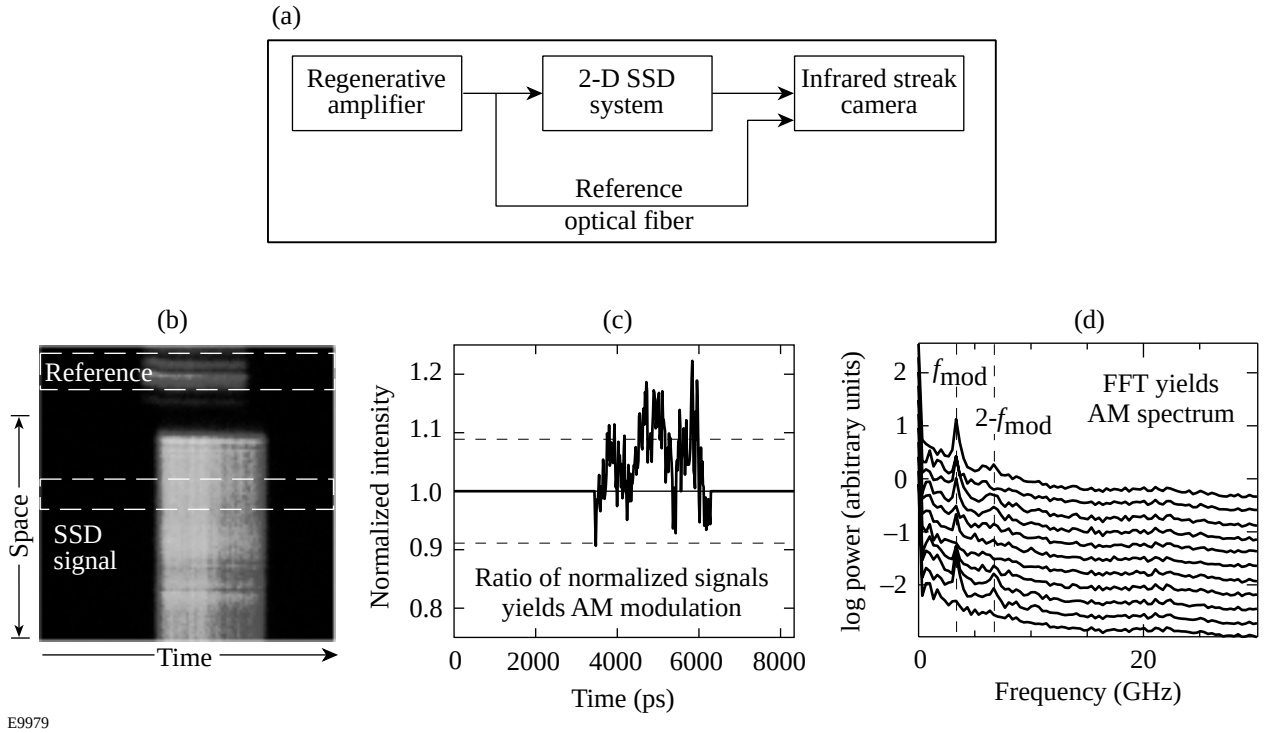

Figure 80.10

An infrared streak camera was employed to identify and measure sources of FM-to-AM conversion. (a) Streak camera measurements of FM-to-AM conversion were performed by comparing the pulse shape at the image plane of the SSD gratings after the SSD system to the pulse shape injected into the 2-D SSD system that is sampled by an optical fiber. (b) The SSD region is divided into regions, and average row lineouts are calculated. A reference pulse shape from the optical fiber delayed input is also acquired. The SSD and reference signals are energy normalized and aligned in time. (c) The ratio of each SSD signal to the reference is used to measure the FM-to-AM conversion. The peak-to-valley in a 333-ps sliding window is calculated for each lineout, and the average value is used as an estimate for the AM. (d) The spectra of the amplitude modulation for a number of different image conditions shown in Fig. 80.11(a) show peaks at the modulation frequency (3.3 GHz) as well as the second harmonic (6.6 GHz) when grating imaging is not optimized. An underlying 1/*f*-like noise spectrum is evident that limits the minimum measurable AM even when no SSD is applied to the beam.

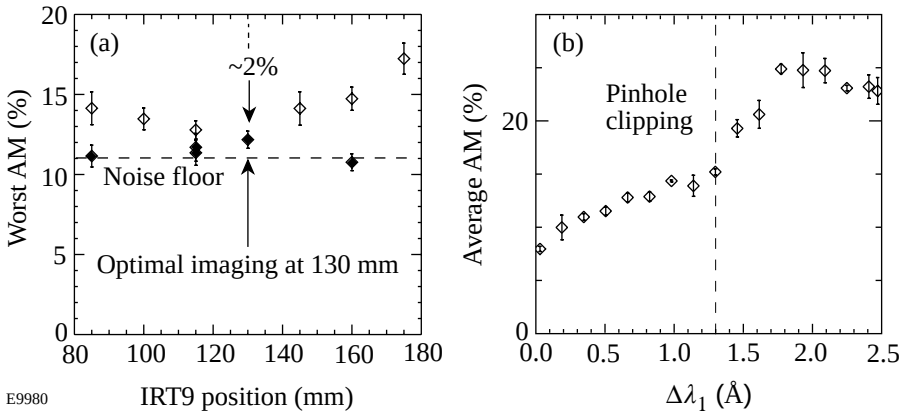

Figure 80.11
AM measurements described in Fig. 80.10 are used to optimize the 2-D SSD system performance. (a) SSD grating imaging is set by minimizing amplitude modulation. Measured AM grows linearly as a function of image plane separation, except near the noise floor where it adds in quadrature with the noise. (b) The onset of pinhole clipping in the slotted LARA spatial filter (1.0×1.8 mm) is characterized by scanning bandwidth produced by the first modulator. The final slotted pinhole dimensions (1.0×2.4 mm) were set to accommodate the specified 1.5 Å, plus extra margin for operational tolerances.

The length of the major axis of the slotted LARA spatial-filter pinhole was also established using this method, as shown in Fig. 80.11(b). The bandwidth generated by the first SSD modulator is dispersed before the LARA. As bandwidth is increased for a given pinhole size, pinhole clipping causes the measured AM values to increase rapidly. For a 1.0×1.8-mm pinhole, clipping is first observed at a bandwidth of approximately 1.3 Å. The final slotted pinhole (1.0×2.4 mm) should maximize spatial-filtering effects while maintaining reasonable operational tolerances.

Summary

Direct-drive ICF experiments require a laser system with excellent irradiation uniformity. Major elements of LLE's beam-uniformity program have been completed, including demonstration of a 10.4-Ghz bulk-phase modulator capable of producing either large SSD bandwidths or multiple color cycles, implementation of a flexible double-pass 2-D SSD architecture, and diagnostics for quantifying the performance of these improved smoothing techniques. The remaining elements of this program will be completed when broadband (1-THz) 2-D SSD is implemented on OMEGA later this year.

ACKNOWLEDGMENT

This work was supported by the U.S. Department of Energy Office of Inertial Confinement Fusion under Cooperative Agreement No. DE-FC03-92SF19460, the University of Rochester, and the New York State Energy Research and Development Authority. The support of DOE does not constitute an endorsement by DOE of the views expressed in this article.

REFERENCES

1. S. Skupsky and R. S. Craxton, Phys. Plasmas **6**, 2157 (1999).
2. S. Skupsky, R. W. Short, T. Kessler, R. S. Craxton, S. Letzring, and J. M. Soures, J. Appl. Phys. **66**, 3456 (1989).
3. A. Babushkin, J. H. Kelly, C. T. Cotton, M. A. Labuzeta, M. O. Miller, T. A. Safford, R. G. Roides, W. Seka, I. Will, M. D. Tracy, and D. L. Brown, in *Third International Conference on Solid State Lasers for Application to Inertial Confinement Fusion*, edited by W. H. Lowdermilk (SPIE, Bellingham, WA, 1999), Vol. 3492, pp. 939–943.
4. J. M. Auerbach *et al.*, Appl. Opt. **18**, 2495 (1979).
5. I. F. Stowers and H. G. Patton, in *Laser-Induced Damage in Optical Materials: 1977*, edited by A. J. Glass and A. H. Guenther, Natl. Bur. Stand. (U.S.), Spec. Publ. 509 (U.S. Government Printing Office, Washington, DC, 1977), pp. 440–454.
6. W. W. Simmons and W. E. Warren, *Laser Program Annual Report 1978*, Lawrence Livermore National Laboratory, Livermore, CA, UCRL-50021-78, **2**, 7-111 (1978).
7. D. C. Brown, in *High-Peak-Power Nd:Glass Laser Systems*, edited by D. L. MacAdam, Springer Series in Optical Sciences (Springer-Verlag, Berlin, 1981), Chap. 7.
8. J. E. Murray *et al.*, in *Solid-State Lasers for Application to Inertial Confinement Fusion (ICF)*, edited by W. F. Krupke (SPIE, Bellingham, WA, 1995), Vol. 2633, pp. 608–614.

The Effect of Pulse Shape on Laser Imprinting and Beam Smoothing

Inertial confinement fusion (ICF) targets are inherently hydrodynamically unstable;[1–3] as a result, perturbations in the target shell can grow exponentially because of Rayleigh–Taylor (RT) instability.[4] For high-convergence implosions it is important to minimize target perturbations and their growth. In direct-drive ICF, nonuniformities in the drive laser produce pressure perturbations that cause mass and velocity perturbations in the target. These "imprinted" perturbations seed the RT instability and ultimately disrupt the implosion. To minimize imprinting, the drive laser must be as uniform as possible. This requires complex laser beam–smoothing techniques.[5] In many ICF target designs the temporal shape of the drive is determined by compression hydrodynamics and thermodynamics (stability and isentrope) and not necessarily to minimize imprint. It is therefore important that the effect of temporal pulse shape on imprinting and beam smoothing be measured and understood. Various experiments have measured imprinting[6–12] and have used control perturbations to normalize the results.[10,12] The experiments reported here are the first to demonstrate the pulse shape's effect on imprinting.

A series of experiments on the OMEGA laser system[13] measured imprinting efficiency using preimposed modulations on planar targets to calibrate the imprint level. The imprinting produced by different temporal pulse shapes and beam-smoothing techniques is compared. Rapidly rising (~100 ps/decade) pulses produce less imprint than pulses with ~1-ns rise time when no temporal beam smoothing is employed. Furthermore, the effect of smoothing by spectral dispersion (SSD)[5] is less pronounced for these rapid-rise pulses. These observations are consistent with plasma smoothing[14] by thermal conduction and differences in the rate at which each pulse produces plasma early in the laser–target interaction.

Imprinting occurs when drive nonuniformities produce pressure perturbations at the target surface that, in turn, produce velocity and mass perturbations at the ablation surface where the RT instability occurs. Laser energy is absorbed in the region outside the critical surface and conducted axially to the ablation surface. If sufficient depth of plasma is present, lateral thermal conduction can provide smoothing of the deposition nonuniformities, thus ending imprinting.[14] Previous simulations[15,16] have investigated imprinting and have indicated that, for a given laser wavelength, imprint efficiency depends linearly on $\delta I/I$ for the intensities relevant to ICF (i.e., $\delta m \propto \delta I/I$), but the duration of imprinting varies depending on the plasma smoothing. Numerical simulations described below show that the condition for smoothing a perturbation of wavelength k is that $kd_c \sim 2$, where d_c is the distance between the ablation surface and a central location in the energy deposition profile.[10] As that thermal conduction region grows, longer wavelengths can be smoothed; thus, for each wavelength the duration of laser imprinting and its total magnitude depends on the time to develop a sufficiently sized conduction zone. Since a slowly rising pulse produces a plasma at a slower rate, imprinting occurs over a longer time, resulting in a higher imprint level in the absence of beam smoothing. The plasma formation rate therefore affects the wavelength dispersion of smoothing. For a given wavelength of interest, imprinting ultimately ceases when the conduction region grows to a sizable fraction of that wavelength. When kd_c is about 2, d_c is about one-third the wavelength of the perturbation. To check the wavelength dependence, the imprint levels of both 30- and 60-μm wavelengths were measured. These correspond to ℓ-modes of 50 and 100 on mm-sized targets, which are pertinent to direct-drive ICF and are in the linear RT growth regime during these measurements.

In these experiments, 20-μm-thick CH (ρ = 1.05 g/cm^3) targets with preimposed modulations were irradiated at 2×10^{14} W/cm^2 by six overlapping UV beams from the OMEGA laser. Target nonuniformities were measured using through-foil x-ray radiography.[17] Experiments were performed with two laser pulse shapes: a 3-ns square (in time) pulse and a 3-ns ramp pulse. The square pulse had a rise time of 100 ps per decade of intensity and an intensity of 2×10^{14} W/cm^2. The ramp pulse rose linearly from ~10^{13} to 2.5×10^{14} W/cm^2 in 3 ns. The latter pulse had a 100 ps/decade

rise to ~10^{13} W/cm^2 before the ramp commenced. For each pulse shape, experiments were performed with and without 2-D SSD beam smoothing.

The driven targets were backlit with x rays produced by a uranium backlighter irradiated at 2×10^{14} W/cm^2 (with 11 additional beams). X rays transmitted through the target and a 3-μm-thick Al blast shield were imaged by a framing camera with 8-μm pinholes filtered with 20 μm of Be and 6 μm of Al. This yielded the highest sensitivity for average photon energy of ~1.3 keV.[17] The framing camera produced eight temporally distinct images of ~100-ps duration and a magnification of 12. The use of optical fiducial pulses, coupled with an electronic monitor of the framing-camera output, provided a frame-timing precision of about 70 ps.

Unfortunately laser imprint cannot easily be measured directly, so measurements often rely on some level of RT growth to produce detectable signals. Targets with low-amplitude, single-mode initial perturbations are used here to provide a calibration from which the initial amplitude of laser imprinting was determined. The basis of this calibration is that in the linear regime the imprinted perturbations ultimately experience similar unstable RT growth to those of preimposed modulations.[8] Although imprinting also produces velocity perturbations, it is useful to assign an equivalent surface roughness to imprinting. This "mass equivalence" is used as a measure of the imprint. The mass equivalence is found by extrapolating the temporal evolution of the imprinted amplitudes back to $t = 0$ by measuring the ratio of the amplitudes of the imprinted and preimposed modes after RT growth has occurred. This requires that the RT instability for those modes remain in the linear regime and do not experience saturation or nonlinear effects.[18] Saturation of RT growth is discussed at length in Ref. 19, where it was shown that at $\lambda = 60$ μm, both the single-mode and the imprinted perturbations behaved linearly for our experimental conditions and observation times. The 30-μm-wavelength imprinting data was measured before the onset of saturation.[19]

The mass equivalence[15] for a specific wave number can be defined as

$$A_{\text{eq}}(k,0) = \left[A_{\text{imprint}}(k,t)/A_{\text{pre}}(k,t)\right]A_{\text{pre}}(k,0), \qquad (1)$$

where $A_{\text{imprint}}(k,t)$ is the measured amplitude of the imprinted features, $A_{\text{pre}}(k,t)$ is the measured amplitude of the preimposed modulation, and $A_{\text{pre}}(0)$ is the known initial amplitude of the preimposed modulation. Using the measurements of the laser nonuniformity, a measure of imprint efficiency[15] is defined as

$$\eta_i(k) = \frac{A_{\text{eq}}(k,0)}{(\delta I/I)},$$

where $\delta I/I$ is the fractional irradiation nonuniformity at the same wavelength.

The amplitudes of these perturbations are obtained using a Fourier analysis of the radiographed images. The Fourier amplitude of the imprint at a given wavelength is defined as the rms of all mode amplitudes at that wavelength, i.e., those modes at a given radius (centered at zero frequency) in frequency space. (The contribution of the preimposed modulation is not included.) The values are summed in quadrature because they are expected to be uncorrelated since they result from the random speckle in the laser. The analysis box is 300 μm in the target plane; thus, in Fourier space, the pixel size is 3.3 mm^{-1}. The pixels at radius 5±0.5 provide the amplitudes of modes with wavelengths between 55 μm and 67 μm, and those at 10±0.5 pixels provide amplitudes for wavelengths between 29 μm and 32 μm.

The preimposed single-mode modulations are two dimensional and possess localized features along a single axis in the Fourier plane at the spatial frequency of this modulation. Figure 80.12(a) depicts a typical radiographic image from these experiments; note that the vertical preimposed modulations are just visible in the mottled pattern produced by the laser imprint. The 2-D Fourier transform of this image after Weiner filtering[17] is shown as a surface plot in Fig. 80.12(b), where the signals from the preimposed modulations stand out from the broadband imprinted features that populate most of the 2-D Fourier space. Figure 80.12(c) depicts a one-pixel-wide annulus that illustrates how the amplitudes for the imprinting are measured. The ratio of the rms value of these amplitudes to that of the preimposed mode times the initial amplitude is used to determine the mass equivalence of imprinting of the control mode. (The box size is optimized for the preimposed mode, thereby ensuring that all the power in that mode is contained in the single pixel.)

For these experiments a variety of beam-smoothing techniques were used. A single-beam laser with only a distributed phase plate (DPP)[20] and no SSD provides a static speckle pattern with ~80% to 100% nonuniformity in wavelengths from 2 μm to 250 μm.[21] The overlap of six beams reduces this

nonuniformity by ~ $\sqrt{6}$. SSD provides a time-varying reduction of the nonuniformity by continually shifting the DPP pattern on the target. The smoothing rate and the asymptotic smoothing level depend on the 2-D SSD bandwidth, which in this experiment is $\Delta\nu = 0.2\ \mathrm{THz}_{\mathrm{UV}}$. In some cases, distributed polarization rotators (DPR's)[22] were added. These provide an instantaneous $\sqrt{2}$ reduction of nonuniformity[23] by separating each beam into two orthogonally polarized beams that are separated by 80 μm in the target plane.

Figure 80.13 shows the measured mass equivalence (in μm) of imprinting at 60-μm wavelength for all three smoothing conditions for the 3-ns square pulse in a series of shots with similar drive intensities. The temporal axis shows the time at which each frame was taken. The mass-equivalence data separate into distinct sets associated with each uniformity condition and are constant in time. Both observations are expected and confirm the utility of this technique. When the growth of the imprinted features are in the linear regime, they should remain a constant ratio of the amplitude of the preimposed mode, leading to a constant mass equivalence. This quantity's dependence on the initial uniformity produced by the various beam-smoothing techniques indicates the sensitivity of this method. For example, the addition of DPR's to the SSD experiments (open squares) reduces the mass equivalence by the expected factor of $\sqrt{2}$ (shaded squares).

The pulse shape's effect on imprinting was then studied by repeating these measurements with a slowly rising pulse, i.e., with an ~2.5-ns rise to the maximum intensity. Figure 80.14 shows the deduced mass equivalence as a function of time for the two pulse shapes, each with and without SSD. Again the data group according to laser conditions (pulse shape or SSD) and exhibit an approximately constant value over considerable times.

These data show that without SSD the ramp pulse produces about 50% more imprinting (higher mass equivalence) than the square pulse. They also indicate that although SSD produces a greater reduction of imprinting on the ramp pulse, the net imprint level after SSD is about the same for both pulses.

Similar experiments were performed using preimposed modulations with $\lambda = 30$ μm. Table 80.I lists the mass-equivalence results for all the experiments. In addition, the imprint efficiency was calculated for the experiments without SSD using the irradiation nonuniformities reported in Ref. 19. The uniformity results were scaled by the differences in analysis boxes between the radiography ($L = 300$ μm; $\Delta k = 0.021$) and the optical experiments ($L = 440$ μm; $\Delta k = 0.0143$). In addition, the values obtained in Ref. 19 were reduced by $\sqrt{6}$ since these experiments utilized six beams. Thus, $\delta I/I$ was 0.00684 for 30 μm and 0.00493 for 60 μm. Lastly, a factor of 2 was included to relate the complex amplitude for ΔI to the mass equivalence, which was normalized to a real cosine function. Since the SSD produces time-varying uniformity, it is difficult to assign a single number to the uniformity and hence the imprint efficiency is not calculated.

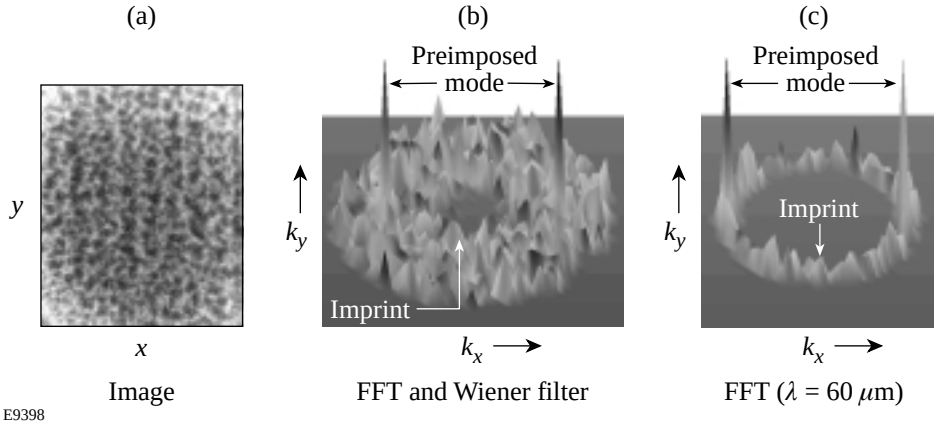

Figure 80.12
(a) Sample of an x-ray radiograph of a target with preimposed 60-μm-wavelength perturbations (vertical striations). The mottled pattern throughout the image is caused by the imprinted features. (b) Representation of the Fourier spectrum of the image in (a), showing the broadband imprinted features as well as two peaks from the preimposed single-mode modulations. (c) The annulus at 55 μm to 68 μm containing two components: the preimposed modulations and the imprinted features. The latter is used as a control feature to gauge the initial amplitude of the imprinted features.

As discussed above, thermal smoothing in the plasma ultimately terminates laser imprint. The duration of imprinting, then, depends on the time required to produce sufficient plasma atmosphere to enable smoothing. One would expect that, compared to the square pulse, the ramp pulse should imprint for a longer duration because the ramp pulse delivers energy at a slower rate and the smoothing plasma is produced more slowly, leading to larger mass equivalence. The imprint efficiencies measured here are lower than those observed by Glendinning *et al.*[12] for a slower rise and lower-intensity ramp pulse, as expected.

Simulations of the experiments were performed with the 2-D hydrodynamics code *ORCHID*[24] to determine the predicted imprint efficiency and the time that pressure perturbations at the ablation surface become negligible as the result of plasma smoothing. The imprint efficiencies were calculated by imposing a single-mode nonuniformity in the laser irradiation. The evolution of the resulting perturbations was compared to that of preimposed mass perturbations of the same wavelength. The experimental temporal pulse shapes were used in the simulations. The simulation results shown in Table 80.I are in reasonable agreement with the measured

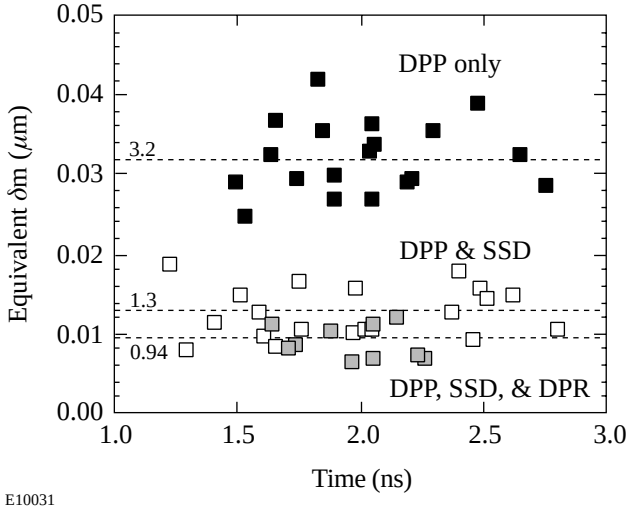

Figure 80.13
The mass equivalence (at 60 μm) derived from planar targets driven by laser beams having a 3-ns square pulse and three types of beam smoothing applied: DPP only (solid), DPP + SSD (open), and DPP + SSD + DPR (shaded). Note that the data segregate according to the laser nonuniformity. The mass equivalence is a measure of the total amount of imprinting, which is seen to decrease as greater beam smoothing is applied.

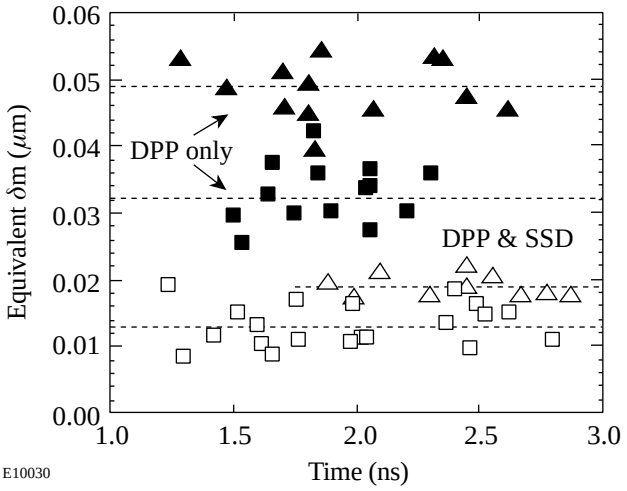

Figure 80.14
The deduced mass equivalence of the imprinted features (at 60 μm) for two pulse shapes: 3-ns square (squares) and ramp (triangles). These data show that for the same laser nonuniformity, a ramp pulse produces more imprinting. The solid and open symbols correspond, respectively, to each of the pulses without and with 2-D SSD. They indicate that the effect of SSD is greater for the ramp pulse, but the net imprint level is similar for the two pulses.

Table 80.I: Mass equivalence and imprint efficiency for various conditions.

Pulse-Shape Uniformity	Mass Equivalence (μm)		Imprint Efficiency: $\delta m/(\delta I/I)$ (μm)			
			Experiment		Simulation	
	60 μm	30 μm	60 μm	30 μm	60 μm	30 μm
Square (no SSD)	0.032±0.005	0.022±0.004	3.3±0.04	1.6±0.03	1.7	1.1
Ramp (no SSD)	0.049±0.008	0.023±0.005	5.0±0.06	1.7±0.04	3.1	2.3
Square (SSD)	0.013±0.003	0.010±0.003				
Ramp (SSD)	0.017±0.005	0.011±0.004				

values. Similar imprint efficiencies were calculated with the 2-D hydrodynamics code *LEOR*.[25] The 2-D simulations underestimate the efficiency at 60 μm, similar to the observations of Glendinning *et al.*[12]

The inherent surface roughness of these foils (transverse to the imposed modulations) was measured to be less than 1% of the imposed mode and, therefore, does not contribute significantly to the error in these measurements. One must consider, however, that the measured signal for the preimposed mode also has a contribution from the imprinted signal at that distinct mode. Since the relative phase of these two signals is arbitrary, the resultant signal can vary significantly when the imprint is a sizable fraction of the preimposed mode, as it is in the no-SSD cases.

Figure 80.15 shows the amplitude of the pressure perturbations (solid curves) at the ablation surface as a function of time for two cases: a ramp pulse and a square pulse, both without SSD. In these simulations a static 60-μm spatial-intensity perturbation of 5% was imposed on the irradiation intensity. Note that the smoothing rate is slower for the ramp pulse and the perturbations persist for a longer period. The temporal evolution (dashed curves) of the conduction zone (d_c) for the two pulse shapes is also shown. This is defined as the distance between the ablation surface and the mean of the energy deposition profile as weighted by a diffusion length: e^{-kz}.

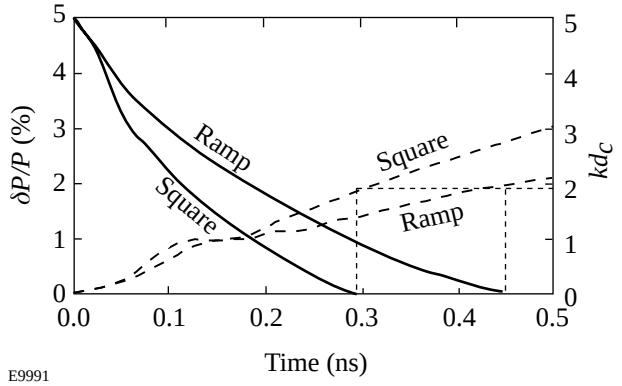

Figure 80.15
The amplitude of perturbations (solid lines) in the ablation pressure (at the ablation surface) as a function of time. The size of the conduction zone (dashed lines) as a function of time in CH targets driven by the square and ramp pulses.These graphs show that imprinting should stop at 300 ps for the square pulse and 450 ps for the ramp pulse. Note that for the square pulse the pressure perturbations are smoothed in 300 ps while for the ramp pulse this occurs at 450 ps.

Imprinting is expected to cease when pressure perturbations at the ablation surface are reduced to negligible levels. Figure 80.15 shows that this occurs for both pulse shapes when d_c ~2. Simple considerations of the distance between critical and ablation surfaces are insufficient to explain the behavior of the two pulses; rather the energy deposition profiles must also be accounted for because considerable smoothing can take place in the plasma region outside the critical surface.

When 2-D SSD is employed, the uniformity at $t = 0$ is the same as without SSD and reduces rapidly in time as $1/\nu$, where ν is the laser bandwidth. For these experiments the UV bandwidth is ~0.2 THz. While at this bandwidth the asymptotic smoothing level for 60 μm is reached in ~1.2 ns,[21] considerable smoothing occurs in less than 400 ps. The experimental results are consistent with this since SSD reduces the imprint for both pulse shapes, although there is greater reduction for the ramp pulse. Since imprinting in the ramp pulse lasts longer, SSD is able to provide greater benefit. The resulting imprint is similar for both pulses with SSD because the effective smoothing time for SSD is shorter than the duration of imprinting for both pulse shapes. Thus, significant SSD smoothing occurs before a large-enough conduction zone is produced. The calculated reduction of the mass equivalence with SSD present is somewhat larger (~60%) than the experimental observations.

This work has shown that for identical nonuniformities, the imprint level depends on the pulse shape, as expected. The total imprinting depends on the irradiation nonuniformity, the imprint efficiency, and the duration of imprint. Since the latter varies with pulse shape and other laser conditions, imprint efficiency cannot be considered invariant. These quantities are also laser wavelength dependent.[10,11] In addition, other processes such as shinethrough and laser–plasma instabilities (filamentation) could alter the intensity distribution within the plasma.

Preimposed modulations have been used as a reference to determine the mass equivalence of features imprinted by a drive laser. This technique behaves linearly under the experimental conditions described here. Slowly rising pulses produce more imprint and experience more smoothing because of SSD than steeply rising pulses. This is a result of the different rates at which smoothing plasma is initially formed, which ultimately determines the duration of imprinting. Numerical simulations confirm this physical picture and yield imprint efficiencies in reasonable agreement with the measured values.

ACKNOWLEDGMENT

This work was supported by the U.S. Department of Energy Office of Inertial Confinement Fusion under Cooperative Agreement No. DE-FC03-92SF19460, the University of Rochester, and the New York State Energy Research and Development Authority. The support of DOE does not constitute an endorsement by DOE of the views expressed in this article

REFERENCES

1. J. Nuckolls *et al.*, Nature **239**, 139 (1972).
2. J. D. Lindl, Phys. Plasmas **2**, 3933 (1995).
3. S. E. Bodner *et al*., Phys. Plasmas **5**, 1901 (1998).
4. G. Taylor, Proc. R. Soc. London, Ser. A **201**, 192 (1950); Lord Rayleigh, Proc. London Math. Soc. **XIV**, 170 (1883).
5. S. Skupsky and R. S. Craxton, Phys. Plasmas **6**, 2157 (1999).
6. M. Desselberger *et al.*, Phys. Rev. Lett. **68**, 1539 (1992).
7. D. H. Kalantar, M. H. Key, L. B. DaSilva, S. G. Glendinning, J. P. Knauer, B. A. Remington, F. Weber, and S. V. Weber, Phys. Rev. Lett. **76**, 3574 (1996).
8. S. G. Glendinning, S. N. Dixit, B. A. Hammel, D. H. Kalantar, M. H. Key, J. D. Kilkenny, J. P. Knauer, D. M. Pennington, B. A. Remington, R. J. Wallace, and S. V. Weber, Phys. Rev. E **54**, 4473 (1996).
9. R. J. Taylor *et al.*, Phys. Rev. Lett. **76**, 1643 (1996).
10. H. Azechi *et al.*, Phys. Plasmas **4**, 4079 (1997).
11. C. J. Pawley *et al.*, Phys. Plasmas **4**, 1969 (1997).
12. S. G. Glendinning, S. N. Dixit, B. A. Hammel, D. H. Kalantar, M. H. Key, J. D. Kilkenny, J. P. Knauer, D. M. Pennington, B. A. Remington, J. Rothenberg, R. J. Wallace, and S. V. Weber, Phys. Rev. Lett. **80**, 1904 (1998).
13. T. R. Boehly, D. L. Brown, R. S. Craxton, R. L. Keck, J. P. Knauer, J. H. Kelly, T. J. Kessler, S. A. Kumpan, S. J. Loucks, S. A. Letzring, F. J. Marshall, R. L. McCrory, S. F. B. Morse, W. Seka, J. M. Soures, and C. P. Verdon, Opt. Commun. **133**, 495 (1997).
14. K. A. Brueckner and S. Jorna, Rev. Mod. Phys. **46**, 325 (1974).
15. S. V. Weber, S. G. Glendinning, D. H. Kalantar, M. H. Key, B. A. Remington, J. E. Rothenberg, E. Wolfrum, C. P. Verdon, and J. P. Knauer, Phys. Plasmas **4**, 1978 (1997).
16. R. J. Taylor *et al.*, Phys. Rev. Lett. **79**, 1861 (1997).
17. V. A. Smalyuk, T. R. Boehly, D. K. Bradley, J. P. Knauer, and D. D. Meyerhofer, Rev. Sci. Instrum. **70**, 647 (1999).
18. S. W. Haan, Phys. Rev. A **39**, 5812 (1989).
19. V. A. Smalyuk, T. R. Boehly, D. K. Bradley, V. N. Goncharov, J. A. Delettrez, J. P. Knauer, D. D. Meyerhofer, D. Oron, and D. Shvarts, Phys. Rev. Lett. **81**, 5342 (1998); V. A. Smalyuk, T. R. Boehly, D. K. Bradley, V. N. Goncharov, J. A. Delettrez, J. P. Knauer, D. D. Meyerhofer, D. Oron, D. Shvarts, Y. Srebro, and R. P. J. Town, Phys. Plasmas **6**, 4022 (1999).
20. Y. Lin, T. J. Kessler, and G. N. Lawrence, Opt. Lett. **20**, 764 (1995).
21. S. P. Regan, J. Marozas, J. H. Kelly, T. R. Boehly, W. R. Donaldson, P. A. Jaanimagi, R. L. Keck, T. J. Kessler, D. D. Meyerhofer, W. Seka, S. Skupsky, and V. A. Smalyuk, "Experimental Investigation of Smoothing by Spectral Dispersion," submitted to the Journal of the Optical Society of America B. This article also appears in Laboratory for Laser Energetics Review **79**, 149, NTIS document No. DOE/SF/19460-317 (1999). Copies may be obtained from the National Technical Information Service, Springfield, VA 22161.
22. Y. Kato, unpublished notes from work at LLE (1984); Laboratory for Laser Energetics LLE Review **45**, 1, NTIS document No. DOE/DP40200-149 (1990). Copies may be obtained from the National Technical Information Service, Springfield, VA 22161.
23. T. R. Boehly, V. A. Smalyuk, D. D. Meyerhofer, J. P. Knauer, D. K. Bradley, R. S. Craxton, M. J. Guardalben, S. Skupsky, and T. J. Kessler, J. Appl. Phys. **85**, 3444 (1999).
24. R. L. McCrory and C. P. Verdon, in *Inertial Confinement Fusion*, edited by A. Caruso and E. Sindoni (Editrice Compositori, Bologna, Italy, 1989), p. 83.
25. D. Shvarts, U. Alon, D. Ofer, R. L. McCrory, and C. P. Verdon, Phys. Plasmas **2**, 2465 (1995).

The Output Signal-to-Noise Ratio of a Nd:YLF Regenerative Amplifier

A regenerative amplifier (regen) is a common element in a variety of laser systems because of its compactness and ability to significantly boost the energy of an optical pulse with minimal temporal distortion and added noise.[1,2] Net gains of the order of 10^8 are easily obtainable. Noise is the unwanted portion of the optical signal that can originate from stochastic or deterministic processes within the system. For some applications, even small amounts of noise are an important concern. One such application is laser fusion, where an optical pulse with less that 1 nJ of energy is amplified with an overall net gain of approximately 10^{14} to the 60-kJ level, frequency tripled to a 351-nm wavelength, and focused onto fusion targets. In such a system, even a relatively small amount of prepulse signal can be detrimental to target performance; therefore, to minimize the prepulse noise signal it is very important to control and maximize the signal-to-noise ratio (SNR) at every step of the amplification process.

In this article we present measurements of the output SNR (defined as the ratio of the peak power of the amplified signal to the average power of the prepulse noise) of a regen used as the first amplification stage in the OMEGA laser system. We compare our measurements to a simple theoretical model that we developed. We find that the prepulse noise signal in the output of our regen has two main contributions: one is due to the intrinsic noise generated within the regen during the amplification process, as studied previously,[2] and the other is due to the prepulse signal on the optical pulse injected into the regen. Our model of the regen output SNR includes both contributions. We experimentally demonstrate that the regen output SNR can be very high for an injected pulse with low noise. We also demonstrate that, in general, the regen output SNR equals the SNR of the pulse injected into the regen in the limit of strong signal injection. Our measurements are in excellent agreement with our theoretical model.

Theory

The total optical power circulating in the regen evolves according to the equation[3]

$$\frac{dP}{dt} = \gamma P(t) + \gamma N_{se}, \tag{1}$$

where γ is the exponential net gain coefficient, P is the optical power circulating in the regen, and N_{se} is phenomenologically included as the noise power in the regen due to spontaneous emission. Equation (1) can be integrated to give

$$P(t) = G P_0 + G N_{inj} + N_{se}(G-1), \tag{2}$$

where $G = \exp(\gamma t)$ is the net gain of the regen, P_0 is the signal power injected into the regen, and

$$N_{inj} = \frac{P_0}{SNR_{in}} \tag{3}$$

is the noise on the signal injected into the regen with SNR_{in} the signal-to-noise ratio of the signal injected into the regen.

It is instructive to describe each term on the right-hand side of Eq. (2). The first term simply represents amplification of the injected signal into the regen and is the regen output signal in the absence of noise. The second and third terms are noise terms. The second term is the amplified injected noise power that describes the amplification of the noise injected into the regen with the optical pulse. The third term is due to the amplification of the spontaneous emission noise generated by the regen itself. The output SNR of the regen is then given by

$$SNR_{out} = \frac{P_0}{N_{se}(1-1/G) + N_{inj}}. \tag{4}$$

For most cases of practical interest the total net gain is much greater than unity ($G >> 1$). If the injected noise power is much less than the spontaneous emission noise power ($N_{inj} << N_{se}$), the second term in the denominator can be neglected and the output SNR of the regen is proportional to the power injected into the regen. For the case where the injected noise power is

much greater than the spontaneous emission noise power ($N_{inj} >> N_{se}$), the first term in the denominator can be dropped. In this case the output SNR_{out} of the regen equals the injected SNR_{in} and is independent of the amount of injected signal power. This model of the regen output SNR is verified by the experiments described below.

Experimental Results

Experiments have been performed to verify the above theory. The details of the regen operation are given elsewhere.[4,5] A pulse is injected into the regen and allowed to evolve until the circulating pulse energy reaches a threshold value. Losses are then introduced in the cavity to maintain the round-trip gain at unity. Later, the cavity losses are removed, and a *Q*-switched train of amplified pulses separated by the regen cavity round-trip time of 26 ns evolves. In our experiment we define the regen output SNR as the ratio of the peak power of a pulse in the pulse train to the power measured between this pulse and an adjacent pulse (i.e., the interpulse noise). This definition is illustrated schematically in Fig. 80.16.

To measure the output SNR of our regen, a high-contrast (>1000:1) Pockels cell with a 10-ns square transmission function is used to select the output power of the regen at various times in the output-pulse train. The timing of the Pockels cell transmission window is first adjusted to pass a single optical pulse from the regen output. The pulse is attenuated and sent to a photodetector, and the peak voltage of the detector is measured and recorded as the regen signal. The Pockels cell transmission window is then moved in time by 13 ns, which is half the regen round-trip time, in order to measure the interpulse noise power between this pulse and the previous pulse in the regen output-pulse train. The calibrated attenuation is removed from the detector, and the average voltage of the photodetector over a portion (~2 ns) of the 10-ns Pockels cell transmission window is measured and recorded as the regen noise power. The overall bandwidth of our measurement system is approximately 1 GHz. These measurements are made as the power of the injected signal is varied. In this way the regen output SNR is recorded versus the power of the injected signal.

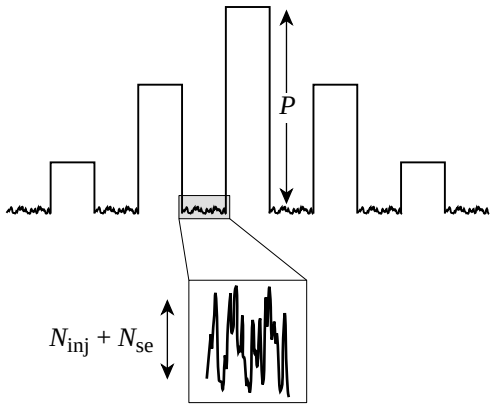

Figure 80.16
Signal-to-noise ratio (SNR) measurement setup. The regen output SNR is defined as the ratio of the power of the injected pulse averaged over a cavity round-trip time to the noise power measured between two regen output pulses.

The pulse injected into the regen is generated with two integrated electro-optic modulators.[6] We apply a square electrical pulse to each modulator synchronous with the transmission through the modulator of an optical pulse from a single-longitudinal-mode (SLM) laser. The transmission function of a dual-channel modulator in this case is given by

$$I_{out}(t) = I_{in}(t)\sin^4\left\{\frac{\pi}{2}\left[\frac{V(t)+V_{dc}}{V_\pi}\right]+\phi\right\}, \qquad (5)$$

where $I_{in}(t)$ is the intensity profile at the modulator input, $V(t)$ is the modulation voltage applied to each channel of the modulator, V_π is the half-wave voltage of the modulator (~10 V), ϕ is a constant phase shift, and V_{dc} is a dc voltage that can be applied to cancel the constant phase shift. Square electrical pulses of 3-ns duration with amplitude V_π are synchronously applied to both channels of the modulator. The short-duration voltage waveforms are applied to the modulator during the peak of the 200-ns Gaussian pulse sent into the modulator from the SLM laser. For this reason, the input-intensity profile to the modulator, $I_{in}(t)$, is assumed to be a constant independent of time. The resulting 3-ns square optical pulse from the modulator is injected into the regen.

A dc bias voltage (V_{dc}) is applied to the modulators to compensate the constant phase term in Eq. (5). When optimally compensated in this way, the modulators provide "zero" transmission for zero applied modulation voltage. This results in a high-contrast pulse (that is, very low prepulse signal) from the modulator. For our experiments, we alter SNR_{in} of the pulse

injected into the regen by changing the dc bias voltage (V_{dc}). As the dc bias voltage is varied away from the high-contrast value, light from the SLM laser leaks through the modulator prior to and after the 3-ns optical pulse. The ratio of the peak power in the 3-ns optical pulse from the modulator to the prepulse (postpulse) power from the modulator is our definition of the SNR_{in} of the pulse injected into the regen. With this definition, the SNR_{in} depends only on the dc-applied voltage to the modulators and is calculated from Eq. (5). This prepulse and postpulse power injected into the regen is the nature of the regen interpulse noise given by the second term in the denominator in Eq. (4). Varying the dc-applied voltage to the modulators varies the SNR of the injected pulse into the regen. The injected power into the regen is varied by attenuating the optical pulse at the input to the modulator.

Measurements of the output SNR of a regen versus the injected power into the regen are shown in Fig. 80.17. For the three curves, the injected SNR was varied as indicated. Using Eq. (4), plots of the regen output SNR are overplotted with the data. To obtain best fits to the data we used 375 nW for N_{se} in all plots, and to determine SNR_{in} we used our measured dc voltages applied to the modulators in Eq. (4). As seen in Fig. 80.17, our measurements are in excellent agreement with theory.

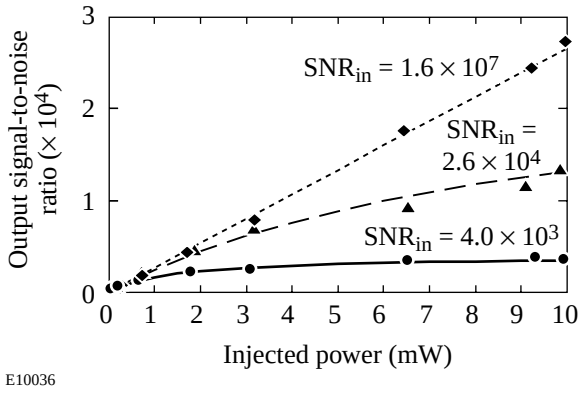

Figure 80.17
Signal-to-noise ratio measurements at the output of a regen versus the injected power into the regen for three values of the SNR of the injected power into the regen.

Separate measurements were made to estimate the amount of equivalent spontaneous-emission noise power, N_{se}, in the regen. A pulse was injected into the regen and the buildup time for the pulse to reach a power level of ~100 W in the regen was measured for different power levels of the injected signal. In Fig. 80.18 the average power of the injected pulse is plotted on a semi-log scale versus the buildup time in the regen. From Eq. (2) and $G >> 1$ the time t_1 for the regen output power to reach a fixed predetermend power level P_1 is given by

$$t_1 = \frac{\ln P_1 - \ln\left(P_0 + N_{inj} + N_{se}\right)}{\gamma}. \qquad (6)$$

When the injected signal power into the regen is much greater that the spontaneous-emission noise power ($P_0 >> N_{se}$), the buildup time t_1 exhibits an exponential dependence on the injected power P_0. The logarithmic fit to the experimental data points in Fig. 80.18 reveals good agreement with this theory. From this logarithmic fit we can estimate N_{se} by using the measured buildup time of 789 ns for the case with no signal injected into the regen. From this we estimate N_{se} to be approximately 80 nW, which is within a factor of 5 of the 375-nW value that was used to obtain the best fit to our data in Fig. 80.17.

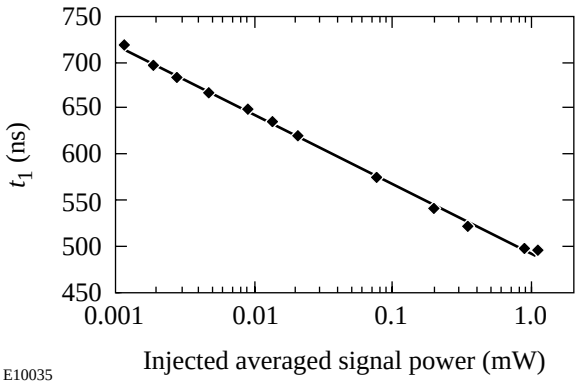

Figure 80.18
Measured time t_1 required for the regen output to reach a preset power level versus averaged power of the pulse injected into the regen. The power of the injected pulse was averaged over one regen round-trip.

Conclusions

We measured the output SNR of a regen and compare our measurements to a simple model that we developed. We show that the noise in the output of a regen has two contributions: one is due to amplified spontaneous emission; the other is due to noise (in our case in the form of a prepulse) injected into the regen. We simulate noise on the input pulse to the regen and conclude from our measurements that the regen output SNR saturates to the SNR of the pulse injected into the regen. We measured an output SNR from the regen as high as 2.7×10^4.

ACKNOWLEDGMENT

This work was supported by the U.S. Department of Energy Office of Inertial Confinement Fusion under Cooperative Agreement No. DE-FC03-92SF19460, the University of Rochester, and the New York State Energy Research and Development Authority. The support of DOE does not constitute an endorsement by DOE of the views expressed in this article.

REFERENCES

1. W. H. Lowdermilk and J. E. Murray, J. Appl. Phys. **51**, 2436 (1980); **51**, 3548 (1980).

2. W. Koechner, *Solid-State Laser Engineering*, 3rd rev. ed., Optical Sciences Series, Vol. 1 (Springer-Verlag, New York, 1992).

3. A. Yariv, *Optical Electronics*, 4th ed. (Saunders College Publishing, Philadelphia, 1995).

4. A. Babushkin, W. Bittle, S. A. Letzring, M. D. Skeldon, and W. Seka, in *Third International Conference on Solid State Lasers for Application to Inertial Confinement Fusion*, edited by W. H. Lowdermilk (SPIE, Bellingham, WA, 1999), Vol. 3492, pp. 124–130.

5. M. D. Skeldon, A. Babushkin, W. Bittle, A. V. Okishev, and W. Seka, IEEE J. Quantum Electron. **34**, 286 (1998).

6. Modulator technical data at http://www.crisel-instruments.it/alemia/html/index01.htm.

Development of New Magnetorheological Fluids for Polishing CaF_2 and KDP

Magnetorheological finishing (MRF) is a novel and recently commercialized[1] process for figuring and polishing plano, convex, and concave optics—both spherical and aspherical—from a wide variety of optical materials. A recently written review article provides an overview of the history, theory, and implementation of this technology.[2] The utility and productivity of MRF have been proven for a wide spectrum of optical glasses and demonstrated for a variety of non-glass optical materials.[3,4] A 1.0-nm smoothness with removal rates of 1 to 10 μm/min is routinely achieved. Seven years of research and development culminated in 1998 with QED Technologies' introduction of a commercial MRF machine, designated the Q22. A focus of continuing research is the development of MR fluid compositions and operating parameters to finish optical materials with an ever-widening range of physical properties. Efforts are simultaneously made to extend our understanding of the fundamental mechanisms of material removal in the MRF process. Extremely hard, extremely soft, single-crystal, polycrystalline, or water-soluble optical materials—each presents unique challenges to the MRF process.

A magnetorheological (MR) fluid is a suspension of magnetically soft ferromagnetic particles in a carrier liquid. Typically, the particles are of the order of a few microns in diameter, and their volume concentration is 30% to 40%. When exposed to a magnetic field, the viscosity and yield stress of the suspension increase several orders of magnitude. The transition is rapid and reversible. The magnetically soft media used to manufacture MR fluids, which are subsequently used in MRF, are carbonyl iron (CI) powders. They are prepared by decomposing iron pentacarbonyl,[5] resulting in spherical particles of almost pure iron, typically 2 to 6 μm in diameter. Incorporating nonmagnetic polishing abrasives results in an MR polishing fluid that can be manipulated to form a renewable and compliant sub-aperture lap for optical finishing.

MRF Research Platforms and Polishing Spots

The Center for Optics Manufacturing (COM) has two research platforms to facilitate the continuing research of MRF: The first, commonly known as the horizontal trough machine, was the basis of the first prototype MRF machine (described and shown in Fig. 1 of Ref. 2), which is still routinely used but without the fluid circulation system. The MR fluid resides in a rotating horizontal trough. The test optic must be spherical convex. While technically overshadowed by newer machines, it continues to be very productive. Experiments can be conducted with only about 100 ml of MR fluid. In addition, the machine can be quickly cleaned to prepare for another experiment. This is particularly useful for screening experiments of new nonaqueous compositions.

A new research platform, designated the spot-taking machine (STM), was designed and constructed by QED Technologies and installed at COM in August 1998 (a photograph of this machine is shown in Fig. 80.19). The MR fluid circulation and conditioning system and rotating wheel are identical to that of the commercial MRF machine. The electromagnet and pole pieces are the same as those on the Q22 with one exception: the pole pieces on the Q22 are tapered downward when moving away from the center to create more clearance when polishing concave optics. The conditioner mixes the MR fluid, maintains its temperature, and monitors and controls its viscosity.

The fluid, typically at an apparent viscosity between 0.04 and 0.1 Pa•s (40 to 100 cps, at a shear rate of ~800 s^{-1}), is delivered through a nozzle by a peristaltic pump onto the surface of the vertical rotating wheel moving at approximately 1 m/s. The wheel is a section of a 150-mm-diam sphere. As the MR fluid ribbon is carried into the magnetic field, the fluid viscosity increases approximately three orders of magnitude in a few milliseconds and becomes a Bingham plastic fluid.[1,2] The high gradient of the magnetic field has the effect of segregating a portion of the nonmagnetic polishing abrasive to the upper layer of the polishing ribbon.[1,6] The surface of the optic is inserted typically 0.5 mm into the ribbon at this point on the wheel, forming a continuously renewed compliant subaperture lap. After flowing under the optic, the wheel carries the fluid out of the magnetic field, where it returns to its original low-viscosity state. A collection device removes the

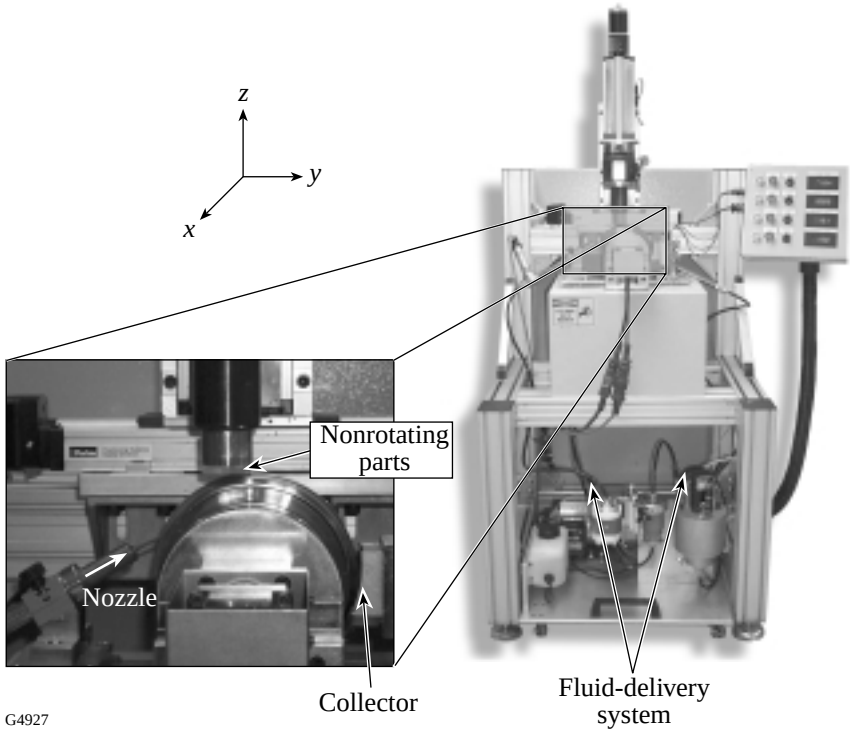

Figure 80.19
A new MRF research platform, the spot-taking machine, incorporates the same fluid-delivery system and vertical wheel as the commercial MRF machine.

fluid from the wheel and returns it to the conditioning system. A typical charge for the system is 1 liter of fluid, which lasts for two weeks of operation.

The STM has a single *z*-axis controller (see Fig. 80.19) to position a test flat into the ribbon for a programmed length of time, typically just a few seconds, and then remove it. The *y*-axis position (parallel to the ribbon) and spindle rotation can be manually adjusted to put multiple spots on a given test flat. The small volume removed, measured interferometrically, is called a "spot" or removal function. Figure 80.20 shows examples of interferograms of spots on two test flats.

By analyzing spots made with these two research platforms we can make critical evaluations on candidate MR fluid compositions. The dimensions of the spots can be measured interferometrically[7] to calculate material-removal rates and measure spot profiles. The surface texture within the spot can be optically profiled[8] to quantify microroughness and reveal surface defects. This information is then used to make informed decisions regarding changes to the fluid composition and/or machine parameters. In addition, the fluid is observed to see that it can be successfully pumped through the delivery system and that it forms a stable ribbon.

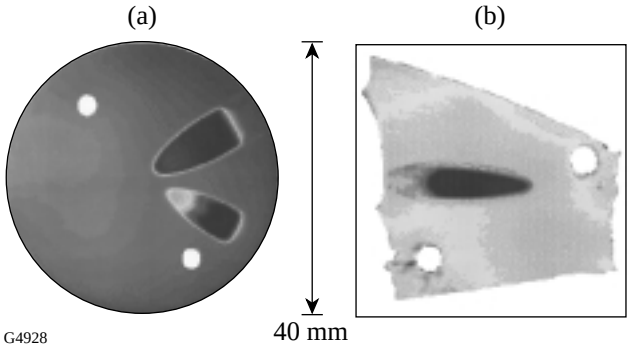

Figure 80.20
(a) An example of an interferogram of two spots made on a CaF_2 test flat. (b) An interferogram of a spot made on a shard broken from a larger plate of KDP. Fiducial marks are used to align interferograms of the original and spotted test flat. Subtraction of the original from the spot interferogram gives the removal function.

One advantage of MRF is the range of operating parameters that can be manipulated to influence the characteristics of the removal function. These include

- MR fluid composition: Carbonyl iron type and concentration, nonmagnetic abrasive type and concentration, carrier fluid and stabilizers can all be adjusted. For aqueous compositions, the MR fluid viscosity can be changed in real-time by adding or removing water.

- Magnetic field: Increasing the magnetic field increases both the stiffness of the ribbon and the removal rates. The practical upper limit is near the saturation magnetization of the magnetic particles. The practical lower limit is where the ribbon is not held tightly against the wheel, resulting in uneven flow under the optic.

- Wheel speed: The removal rate is proportional to the wheel speed. A typical value is 150 rpm but it can be varied from 100 to 400 rpm (0.79 to 3.15 m/s, 150-mm-diam wheel).

- Nozzle: Nozzles with different diameter and shaped orifices can be installed. The standard nozzle is circular and 3 mm in diameter.

- Ribbon height: Increasing the flow rate, typically between 0.5 and 1.0 liter/min, increases the height, or thickness, of the ribbon for a given wheel speed. A typical height is 1.0 to 2.0 mm.

- Depth (inversely, gap): Decreasing the gap between the optic and the wheel increases the depth of penetration into the ribbon and increases the area, or footprint, of the spot.

This range of operating conditions permits many options when conducting experiments on a wide variety of optical materials.

MRF of CaF_2 and KDP

In this article we present details of recent work to adapt MRF to two soft, single-crystal optical materials: calcium fluoride, CaF_2, and potassium dihydrogen phosphate, KH_2PO_4 or KDP. It was necessary to formulate two new magnetorheological fluid compositions in order to successfully apply MRF to these two materials. The standard MR fluid, suitable for a wide variety of optical materials, consists of (in vol %) 36% CI, 55% water, 6% cerium oxide, and 3% stabilizers. CaF_2 is incompatible with the standard MR fluid typically used for optical glasses, resulting in "sleeks" and unacceptable roughness. KDP is extremely water soluble and therefore also cannot be finished with the standard aqueous MR fluid. Some mechanical properties for these two materials are compared to typical optical glasses in Table 80.II.

Results with CaF_2

Single-crystal calcium fluoride is the optical material that is expected to meet the projection and illumination requirements for photolithography optics as the semiconductor industry begins the transition from 365 and 248 nm to 193 and 157 nm.[15] CaF_2 crystals are fairly soft, so the polishing technique used must carefully reduce surface roughness without creating surface sleeks or fine scratches. These defects can lead to scattering, subsurface damage, and microscopic flaws in a coated surface.[16] In addition, CaF_2 is thermally sensitive, anisotropic, and easily chipped. Manufacturing large optics, such as 100-mm catadioptic cubes or 400-mm refractive lenses, by conventional means is nontrivial.[17,18] A $\lambda/10$ flatness specification at 193 nm is more than three times tighter than a $\lambda/10$ specification at 633 nm.[18] Fortunately, as discussed elsewhere,[2] one of the greatest strengths of MRF is its ability to deterministically finish optics to very high precision.

Table 80.II: Physical properties of CaF_2 and KDP compared to typical optical glasses.

Material	Source	Structure	Water solubility (g/100 g)	Near-surface hardness (GPa)	Young's modulus (GPA)	Fracture toughness (MPa-$m^{0.5}$)
KDP	Cleveland Crystals, Inc.	single-crystal tetragonal, type-II cut	33 (Ref. 10)	2.16 (Ref. 14)	49.2 (Ref. 14)	0.1-0.2 (Ref. 13)
CaF_2	Optovac, Inc.	single-crystal cubic c-cut	0.0017 (Ref. 9)	2.47 (Ref. 14)	110 (Ref. 12)	0.33 (Ref. 12)
BK-7	Schott, Ohara	glass	insoluble	7.70 (Ref.14)	79.6 (Ref. 14)	0.85 (Ref. 11)
Fused silica	Corning	glass	insoluble	9.79 (Ref. 14)	74.7 (Ref. 14)	0.75 (Ref. 11)

The initial strategy for developing an MR fluid for polishing CaF_2 called for the replacement of cerium oxide as the nonmagnetic abrasive and making the fluid more gentle due to the softness of this material. Toward this end, many fluid compositions were screened with spot experiments using the horizontal trough machine. For all of the experiments with CaF_2, the test optics were initially pitch polished to an average rms roughness of 0.85±0.05 nm. Compositions containing (in vol %) 36% CI, 25% PEG 200, 38% water, <1% stabilizers, and then a fraction of a percent of nanodiamond powder[19] were tested to determine material-removal rates and microroughness. PEG 200[20] was included because of its lubricious behavior, which was intended to protect the surface from scratching and eliminate embedded particles. Figure 80.21 is a plot of the peak removal rate for a range of nanodiamond concentrations. The removal rate rises quickly with nanodiamond concentration but rolls over above ~0.1 vol %. The roughness values within the generated spots varied from 1.0 to 1.65 nm and showed no clear trend as a function of nanodiamond concentration.

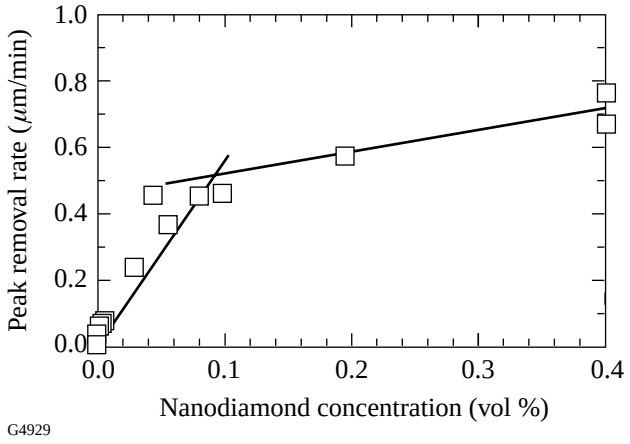

Figure 80.21
Plot of peak removal rate for CaF_2 versus nanodiamond concentration on the trough machine for MR fluid containing 36% CI, 25% PEG 200, 38% water, and <1% stabilizers.

Although it is possible to magnetorheologically finish CaF_2 to low roughness values with compositions containing PEG 200 and nanodiamonds, the very low peak removal rates observed encouraged us to revisit water-based compositions. For this reason, we tested a MR fluid containing (in vol %) 48% CI, 49% water, 3% stabilizers, and ~0.2% nanodiamond powder. This slurry composition had been developed and previously tested for MRF of very hard materials, such as SiC and sapphire, and was found to be rheologically stable. Spots made on the horizontal trough machine at a 3.0-kG magnetic field strength resulted in a very stiff ribbon and very high peak removal rates > 8 μm/min; however, the rms roughness values were consistently ~2.0 nm. Decreasing the magnetic field strength to 0.85 kG decreased the peak removal rate to 1.3 μm/min but also decreased the rms roughness to ~1.25 nm. This indicated that decreasing the magnetic field strength and decreasing the stiffness of the fluid ribbon would produce lower values of surface roughness.

The same composition was next tested in the STM. Spots were made at three levels of magnetic field strength. At a value of 0.34 kG, it was discovered that the ribbon was very soft and formed a large, ill-defined spot. The peak removal rate was an acceptable 1.6 μm/min, but the spot shape was not usable. Increasing the magnetic field strength to 0.98 kG produced a stiffer ribbon and well-defined spot. The resulting peak removal rate was very high, 7.8 μm/min, and the average rms roughness was very good at 1.00±0.06 nm. At 1.85 kG the peak removal rate increased even further to 11.8 μm/min, and the rms roughness was slightly higher at 1.15±0.06 nm. (These results are summarized in Table 80.III.) Extended life testing in the STM and the Q22 confirmed the composition to be sufficiently stable over time for polishing trials.

Table 80.III: Peak removal rate and roughness for MRF spots on CaF_2 at various magnetic field strengths.

Magnetic field (kG)	Peak removal rate (μm/min)	Microroughness
0.34	1.6	poor spot shape
0.98	7.8	1.00±0.06
1.85	11.8	1.15±0.06

Results with KDP

KH_2PO_4, or KDP, is an important electro-optic material. It is currently used for frequency conversion of LLE's OMEGA laser. It will be part of the National Ignition Facility's laser under construction at Lawrence Livermore National Laboratory. It is also commonly used in electro-optic devices such as Pockels cells.[10]

Polishing KDP poses several difficult challenges: KDP is expensive in large sizes. It is difficult to polish high-aspect-ratio KDP flats with conventional pitch-lapping techniques. KDP is extremely soluble in water. To magnetorheologically finish KDP, the MR fluid carrier liquid must be nonaqueous, and it must be possible to clean the MR fluid off of the optic with a KDP-compatible solvent. Finally, KDP is very soft with

a near-surface hardness of 2.16 GPa (Berkovich microindentor, 5-nN load).

Currently, single-point diamond turning (SPDT) is considered state of the art for finishing KDP, yielding surfaces with 1.0- to 3.0-nm rms roughness.[21] This process is capable of producing 30-cm-diam flat plates for use in large laser systems. SPDT is done by showering mineral oil over the workpiece. This provides lubricity for cutting and helps to control temperature. The oil is removed from the KDP surface with toluene or xylene.

Many oil-based MR fluid compositions have been developed for use in mechanical engineering applications.[6] For practical reasons, it is highly desirable to use a carrier fluid that is nonflammable and capable of being cleaned out of a MRF machine with aqueous-based detergents. During the search for an MR fluid for KDP, chemical compatibility issues became a serious concern. A number of tested water-miscible fluids were found to leave a "fog" on the surface of KDP. (Results of compatibility tests are summarized in Table 80.IV.) Even just a few minutes of contact with 200-proof ethanol transfers enough moisture from the air to leave visible defects on the surface of a KDP flat. Several otherwise-promising MR fluid compositions had to be discarded for this reason. After numerous trials, the base composition found to produce the best results with KDP consisted of (in vol %) 40% CI and 60% dicarboxylic acid ester. This carrier liquid has a very low vapor pressure, does not evaporate, and is easily cleaned out of the STM. This nonaqueous MR fluid is shear-thinning with a viscosity of 0.09 Pa•s (90 cps) at a shear rate of 800 s^{-1} (approximately the shear rate for the fluid in the delivery nozzle of the STM).

The results reported in this article were obtained on surfaces of KDP that were initially prepared by single-point diamond turning.[22] The average rms roughness of this initial surface (five measurements over five sites[8]) was 1.5±0.2 nm. A representative optical roughness map of the initial diamond-turned surface is shown in Fig. 80.22. The turning marks are clearly visible.

Spots were first made with the MR fluid without any nonmagnetic abrasive under a fixed set of conditions.[23] An example of profile scans of a spot[7] are shown in Fig. 80.23. The peak removal rate, calculated from a depth of deepest penetration of the spot, 0.53 μm, was 1.59 μm/min. The rms microroughness was increased to 6.4±0.8 nm. Figure 80.24 gives an optical roughness map of the surface within this spot. The grooves from the flow of the MR fluid are clearly visible.

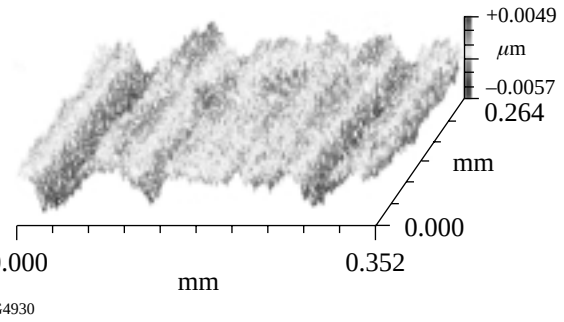

Figure 80.22
Representative optical roughness map[8] of the initial single-point-diamond-turned surface of KDP used for these experiments. The diamond-turning marks are clearly visible. Microroughness: pv = 15.6±3.9 nm; rms = 1.5±0.1 nm.

Table 80.IV: KDP compatibility test results for candidate carrier fluids.

Fluid	Results/Comments
Glycerol	No fogging; viscosity too high for pumping in STM
Ethylene glycol	Serious fogging in just a few seconds of contact
Polyethylene glycol, M.W. 200	Light fogging after several minutes; halo around MRF spots
Liquid paraffin	No fogging in 60 min; oil-based carrier fluid undersirable
Decahydronaphthalene	No fogging; too volatile
Ethanol, 200 proof	Fogging when exposed in air; not in dry N_2; too volatile
Dicarboxylic acid ester	No fogging after extended contact; no halo around spots

The original diamond-turning marks, which would be running approximately perpendicular to the MRF grooves, have been eliminated. The removal rate was in a convenient range, but the goal was not to increase the surface roughness.

Nanodiamond powder[19] was then added to the MR fluid, corresponding to a nominal concentration of 0.05 vol %. The addition of this amount of abrasive had no effect on the MR fluid viscosity. Spots taken with this fluid under the same conditions[23] showed that the peak removal rate increased moderately to 2.10 μm/min. But more importantly, the rms microroughness of 1.6±0.2 was essentially unchanged from that of the initial diamond-turned surface. Figure 80.25 gives a representative optical roughness map of the surface within this spot. The addition of nanodiamonds also decreased the amplitude of the grooves formed by MRF. We expect that these grooves would be eliminated entirely with part rotation during full-scale polishing runs.

The KDP surfaces produced by MRF have been evaluated for laser-damage resistance at LLE. Results are summarized in Table 80.V. MRF maintains the high laser-damage threshold of a diamond-turned KDP part at both λ = 351 nm and λ = 1054 nm.

In light of these encouraging results on KDP with this new slurry composition, the next scheduled task is to scale up to full polish runs on a production MRF machine like the Q22. This will allow a quantitative evaluation of removal efficiency, figure correction capability, and smoothing.

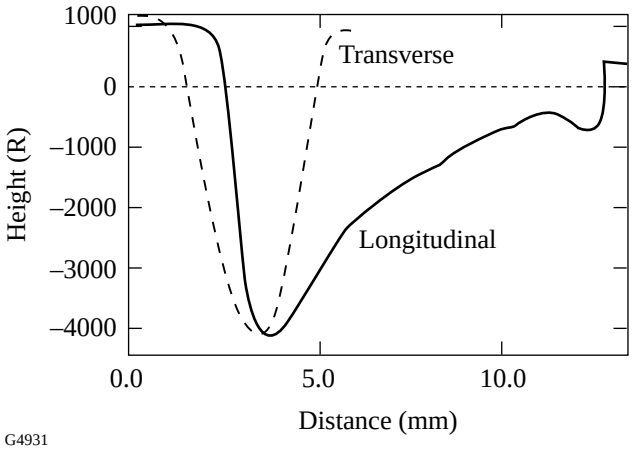

Figure 80.23
Longitudinal and transverse profile scan[7] of a spot made on SPDT KDP with MR fluid without nonmagnetic abrasive. Peak removal rate was 1.59 μm/min; depth of deepest penetration was 0.53 μm.

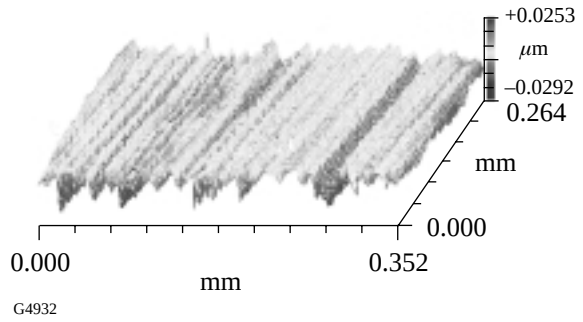

Figure 80.24
Optical roughness map[8] of spot made on SPDT KDP part using MR fluid without nonmagnetic abrasive. Microroughness: pv = 64.8±15.8 nm; rms = 6.4±0.8 nm.

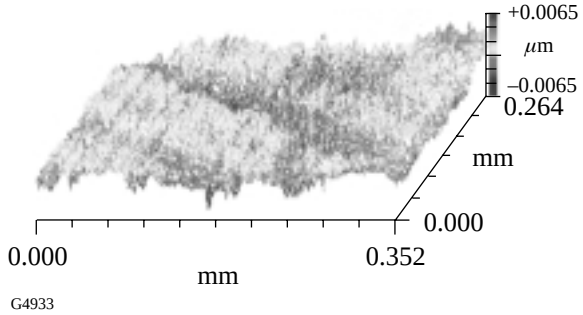

Figure 80.25
Optical roughness map[8] of surface within spot made on SPDT KDP part with MR fluid with 0.05-vol % nanodiamond abrasive. Microroughness: pv = 20.1±7.1 nm; rms = 1.6±0.3 nm.

Summary

This article shows how sub-aperture removal functions, i.e., polishing "spots," are generated on test flats using two magnetorheological finishing (MRF) research platforms. Evaluation of polishing spots is used to further our understanding of MRF and to extend its capabilities to new classes of optical materials. Examples are presented that demonstrate how new MR fluid compositions and operating parameters may be developed for processing CaF_2 and KDP using the evaluation of polishing spots.

ACKNOWLEDGMENT

Support for this work is provided by the Center for Optics Manufacturing, QED Technologies LLC., the U.S. Army Materiel Command, and DARPA.

Table 80.V: Laser-damage test results for KDP parts processed with MRF and SPDT.

J/cm^2	@ 3ω, 1 ns		@1ω, 1 ns	
	1-on-1	N-on-1	1-on-1	N-on-1
MRF	11.23±0.61	14.08±1.06	12.17±1.80	14.76±1.67
Diamond turned	10.63±0.68	14.56±1.08		

REFERENCES

1. D. Golini, Laser Focus World **34**, 187 (1998).
2. D. Golini *et al.*, "Magnetorheological Finishing (MRF) in Commercial Precision Optics Manufacturing," to be published in *Optical Manufacturing and Testing III*, edited by H. P. Stahl (SPIE, Bellingham, WA, 1999), Vol. 3782.
3. D. Golini, S. Jacobs, W. Kordonski, and P. Dumas, in *Advanced Materials for Optics and Precision Structures*, edited by M. A. Ealey, R. A. Paquin, and T. B. Parsonage, Critical Reviews of Optical Science and Technology (SPIE, Bellingham, WA, 1997), Vol. CR67, pp. 251–274.
4. S. D. Jacobs, F. Yang, E. M. Fess, J. B. Feingold, B. E. Gillman, W. I. Kordonski, H. Edwards, and D. Golini, in *Optical Manufacturing and Testing II*, edited by H. P. Stahl (SPIE, Bellingham, WA, 1997), Vol. 3134, pp. 258–269.
5. F. L. Ebenhoech, Prog. Powder Metall. **42**, 133 (1986).
6. B. Berkovski, ed. *Magnetic Fluids and Applications Handbook*, UNESCO Series of Learning Materials (Begell House, New York, 1996), Chap. 6.
7. Zygo Mark IVxp™ or Zygo GPIxpHR™ phase-shifting interferometer systems were used for all data acquisition and analysis related to polishing spots, workpiece surface figure, and transmitted wavefront quality reported in this paper; Zygo Corporation, Middlefield, CT 06455.
8. Zygo NewView™ 100 White Light Optical Profiler, areal over 0.25 mm × 0.35 mm with a 20× Mirau objective, no filter; Zygo Corporation, Middlefield, CT 06455.
9. R. C. Weast, ed. *CRC Handbook of Chemistry and Physics*, 68th ed. (CRC Press, Boca Raton, FL, 1987).
10. J. T. Milek and M. Neuberger, *Linear Electrooptic Modular Materials*, Handbook of Electronic Materials, Vol. 8 (IFI/Plenum, New York, 1972).
11. J. C. Lambropoulos, S. Xu, and T. Fang, Appl. Opt. **36**, 1501 (1997).
12. W. F. Krupke *et al.*, J. Opt. Soc. Am. B **3**, 102 (1986).
13. Value varies with orientation. T. Fang, "Near-Surface Mechanical Properties of Optical Materials in Deterministic Microgrinding," Ph.D. thesis, University of Rochester, 1997.
14. Nano IIs nanoindentor, 5-mN load, Nano Instruments, Oak Ridge, TN 37830; Berkovich indentor.
15. R. DeJule, Semicond. Int. **22** (1), 36 (1999).
16. R. DeJule, Semicond. Int. **22** (2), 38 (1999).
17. R. DeJule, Semicond. Int. **22** (3), 36 (1999).
18. D. Collier and W. Pantley, Laser Focus World **34**, 63 (1998).
19. Dianan® Nano Diamond powder, Straus Chemical Corporation, Elk Grove Village, IL 60007.
20. Carbowax® Polyethylene Glycol 200, Union Carbide Corporation, Danbury, CT 06817-0001.
21. R. C. Montesanti and S. L. Thompson, Lawrence Livermore National Laboratory, Livermore, CA, UCRL-ID-121651 (1995).
22. Cleveland Crystals Inc., Cleveland, OH 44110.
23. Experimental parameters: wheel speed, 150 rpm; magnet current, 15.0 amps (2.22 kG); ribbon height, 2.0 mm; depth into ribbon, 0.5 mm.

LLE's Summer High School Research Program

During the summer of 1999, 12 students from Rochester-area high schools participated in the Laboratory for Laser Energetics' Summer High School Research Program. The goal of this program is to excite a group of high school students about careers in the areas of science and technology by exposing them to research in a state-of-the-art environment. Too often, students are exposed to "research" only through classroom laboratories, which have prescribed procedures and predictable results. In LLE's summer program, the students experience all of the trials, tribulations, and rewards of scientific research. By participating in research in a real environment, the students often become more excited about careers in science and technology. In addition, LLE gains from the contributions of the many highly talented students who are attracted to the program.

The students spent most of their time working on their individual research projects with members of LLE's technical staff. The projects were related to current research activities at LLE and covered a broad range of areas of interest including laser modeling, diagnostic development, chemistry, liquid crystal devices, and opacity data visualization (see Table 80.VI).

The students attended weekly seminars on technical topics associated with LLE's research. Topics this year included lasers, fusion, holography, optical materials, global warming, measurement errors, and scientific ethics. The students also received safety training, learned how to give scientific presentations, and were introduced to LLE's resources, especially the computational facilities.

The program culminated with the High School Student Summer Research Symposium on 25 August at which the students presented the results of their research to an audience including parents, teachers, and LLE staff. The students' written reports will be bound into a permanent record of their work that can be cited in scientific publications. These reports are available by contacting LLE.

One hundred and five high school students have now participated in the program since it began in 1989. The students this year were selected from approximately 80 applicants.

In 1997, LLE added a new component to its high school outreach activities: an annual award to an Inspirational Science Teacher. This award honors teachers who have inspired High School Program participants in the areas of science, mathematics, and technology and includes a $1000 cash prize. Teachers are nominated by alumni of the High School Program. The 1999 William D. Ryan Inspirational Teacher Award was presented at the symposium to Mr. John Harvey of Honeoye Falls–Lima Senior High School. Mr. Harvey, a mathematics teacher, was nominated by Jeremy Yelle and David Rea, participants in the 1997 program. Mr. Yelle wrote, "I have never met another teacher that was so passionate for what he teaches and communicates himself well enough to get even the most complicated of ideas into the simplest of minds." He added, "Mr. Harvey has expanded my interest in science and mathematics not only by opening doors and giving his insight, but also showing me that mathematics can be learned not only in a classroom, but in an open forum, or even in the applications of daily life." Mr. Rea wrote, "I can think of no teacher that has given me a greater gift of learning than Mr. John Harvey." He added, "Mr. Harvey must also be recognized for his dedication to students after the books have closed and the homework has been passed in." Mr. Peter Cardamone, principal of Honeoye Falls–Lima Senior High School, added, "John's excellence in teaching is balanced well with his concern and interest in students under his tutelage."

Table 80.VI: High School Students and Projects—Summer 1999.

Student	High School	Supervisor	Project
Kendra Bussey	Pittsford Sutherland	K. Marshall	Synthesis of Highly Soluble Near-IR Dyes for the Liquid Crystal Point-Diffraction Interferometer
Michael Harvey	R. J. Davis, Livonia	M. Skeldon	Characterization of the Signal-to-Noise Ratio in a Regenerative Amplifier
Peter Hopkins	The Harley School	S. Craxton	Comparing Opacity Data Groups with a Java-Based Graphical User Interface
Jyoti Kandlikar	Brighton	R. Epstein	Statistical Properties of Continuous and Discrete Distributed Phase Plates
Brian Kubera	Webster	R. Boni	Bandwidth Measurement of Fiber Optic Bundles
Aman Narang	The Harley School	W. Donaldson	Spectroscopic Analysis of an OMEGA Beamline
Lutao Ning	Brighton	M. Guardalben	Characterization of the Liquid Crystal Point-Diffraction Interferometer
Rohit Rao	Brighton	S. Craxton	Computer-Aided Modeling of the Liquid Crystal Point-Diffraction Interferometer
Alice Tran	Spencerport	C. Stoeckl	Integrating Hard X-Ray Diagnostics into OMEGA Operations
Jordan VanLare	Victor	K. Marshall	Calculating the Optical and Dielectric Anisotropy of Liquid Crystalline Systems
Jeffrey Vaughan	Fairport	P. Jaanimagi	Correcting Distortion in an X-Ray Streak Camera
Emily Walton	Fairport	J. Knauer	Measurement of Scattered 351-nm Light from OMEGA Targets

FY99 Laser Facility Report

FY99 was a productive year on OMEGA; 1207 shots on target were shared by LLE, LLNL, LANL, and NLUF users (see Table 80.VII). Shot operations were conducted on a 12 h/day, 3 day/week schedule; for many campaigns the standard 1-h cycle time for OMEGA was achieved. Uninterrupted 12-h shot sequences resulted in improved efficiency and effectiveness in completing experimental goals.

The following major system modifications were implemented during FY99:

- Upgrade of 2-D SSD to 0.3-THz bandwidth at three color cycles
- Installation of the majority of the hardware necessary to conduct cryogenic target shots
- Installation of the LLNL Active Shock Breakout (ASBO) diagnostic
- Migration to Oracle™ database systems
- Implementation of second tripler frequency-conversion crystals on beams used for planar experiments
- Installation of two full-aperture backscatter stations
- Replacement of the target chamber roughing systems with dry pumps to support incorporation of a tritium-removal system

Improved individual-beam uniformity resulting from an upgrade of the 2-D SSD system is discussed in the article beginning on p. 197. The modification included removing the first-generation 2-D SSD system from OMEGA and replacing it with a pre-assembled modular unit that included high-frequency, multipass electro-optic modulators. Activation of the new 2-D SSD system went smoothly, and its reliability has been exceptional. Notable features include the flexibility to easily migrate to a full 1.0-THz bandwidth (planned for early FY00), an integrated diagnostic suite, and improved LLE-fabricated holographic optics.

Coincident with the installation of the THz-capable SSD system, second tripler frequency-conversion crystal assemblies were added to 13 of 60 beams. These additional frequency-tripling crystals will provide efficient frequency conversion for laser bandwidths up to the 1-THz level and represent the first stage of a project to modify all 60 beams. With this subset of crystals the planar-foil imprint and Rayleigh–Taylor growth investigations will be extended to higher-uniformity regimes.

The upper and lower pylons of the cryogenic target-handling system (CTHS) were installed on OMEGA. The lower pylon installed on the bottom of the target chamber supports the insertion of targets using the moving cryostat. The upper pylon installed on the target chamber's north pole supports the cryogenic shroud retraction system. The CTHS will be fully activated in FY00.

Table 80.VII: The OMEGA shot summary for FY99.

LLE-RTI	337
LLE-ISE	243
LLE-LSP	62
LLE diagnostic development	85
NLUF	144
LLNL	173
LANL	163
Total	1207

National Laser Users' Facility News

FY99 Experiments

During FY99 significant progress was made on several National Laser Users' Facility (NLUF) projects.

David Cohen and colleagues from the University of Wisconsin at Madison in collaboration with investigators from Prism Computational Sciences, the University of Rochester (UR/LLE), Los Alamos National Laboratory (LANL), Lawrence Livermore National Laboratory (LLNL), and Sandia National Laboratory (SNL) carried out a series of x-ray spectroscopic measurements to explore the physics of radiation-driven, NIF-type ablators.

Hans Griem and colleagues from the University of Maryland conducted experiments using soft x-ray spectroscopy to investigate the plasma conditions at early times in ICF direct-drive capsules.

Bruce Remington, Harry Robey, and colleagues from LLNL in collaboration with investigators from the University of California (UC) at Davis, the University of Arizona, UR/LLE, the University of Chicago, Drexel University, CEA Saclay, Osaka University, State University of New York (SUNY) at Stony Brook, and LANL performed studies of supernova hydrodynamics on OMEGA. These experiments were a continuation of experiments initiated on the Nova laser at LLNL and now being performed on LLE's OMEGA under the NLUF program.

Dan Kalantar and colleagues from LLNL in collaboration with investigators from UC San Diego, the University of Oxford, California Institute of Technology, and LANL carried out studies of the dynamic properties of shock-compressed solids via *in-situ* transient x-ray diffraction.

Richard Petrasso and colleagues from the Massachusetts Institute of Technology (MIT) in collaboration with Stephen Padalino and colleagues from SUNY Geneseo as well as investigators from UR/LLE and LLNL conducted experiments to characterize high-density plasma conditions in imploded ICF capsules using charged-particle spectroscopy on OMEGA. These experiments explored several techniques for measuring fuel and ablator areal densities. The SUNY Geneseo group also carried out a collaborative series of tests to investigate the feasibility of carbon activation as a means of measuring tertiary neutron yield in high-performance OMEGA and NIF ICF capsules.

Charles Hooper and colleagues from the University of Florida along with investigators from the University of Nevada and UR/LLE performed a series of experiments to investigate via x-ray absorption spectroscopy the x-ray emission characteristics of ultrahigh-density plasma.

Bedros Afeyan from Polymath Research in collaboration with colleagues from LLNL, LANL, and UR/LLE carried out experiments to investigate optical-mixing-controlled stimulated scattering instabilities in NIF-like, long-scale-length plasmas.

Figure 80.26 shows an example of work carried out under the FY99 NLUF program; it illustrates the work of a team headed by H. Robey and B. Remington of LLNL to study two aspects of the physics of supernovae. These experiments studied the growth rate of the Richtmyer–Meshkov (RM) and Rayleigh–Taylor (RT) instabilities of a perturbation seeded by the arrival of a rippled shock wave on an initially unperturbed interface. Figure 80.26 shows images demonstrating the time evolution of the shock structure of a laser-driven, planar, copper ablator and a CH payload. In these experiments, the Cu/CH interface had an imposed perturbation wavelength of 200 μm, and the Cu ablator was driven with ~3 kJ in a square-top, 1-ns pulse. A separate x-ray backlighter and an x-ray framing camera were used to obtain the x-ray radiographs of Fig. 80.26. The backlighter pulses were also 1 ns long but delayed by up to 78 ns relative to the drive pulses.

In FY99 a total of 144 OMEGA target shots were dedicated to the NLUF program. In addition to NLUF-supported programs, several direct- and indirect-drive experiments, also

coordinated through the NLUF Manager, were carried out on OMEGA by groups from LLNL and LANL. These experiments included campaigns on direct-drive cylinders, hohlraum symmetry, equation of state, RM and RT instabilities, tetrahedral-hohlraum implosions, double-shell targets, diagnostics development, radiation flow, opacity, and other topics. The variety of FY99 experiments is best illustrated by Fig. 80.27, which shows examples of targets shot on OMEGA during the fiscal year.

FY00 Proposals

Thirteen proposals were submitted to NLUF for FY2000. A DOE technical evaluation panel chaired by the NLUF Manager and including Dr. David Bradley (LLNL), Dr. David Montgomery (LANL), Dr. Ramon Leeper (SNL), and Dr. Ned Sautoff (PPPL) reviewed the proposals at a meeting held on 26 May 1999 and recommended approval of seven proposals for funding (see Table 80.VIII).

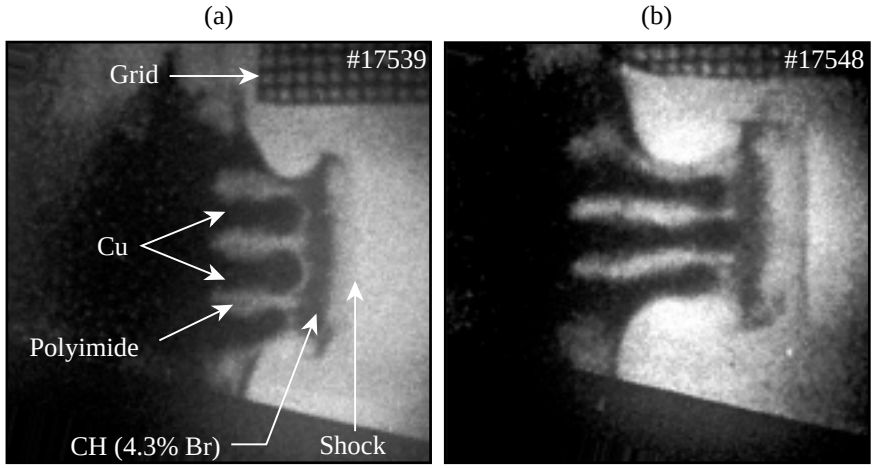

Figure 80.26
Two x-ray-backlighted images from two SNRT #1 experiments showing the time evolution of the shock and instability structure at late times.

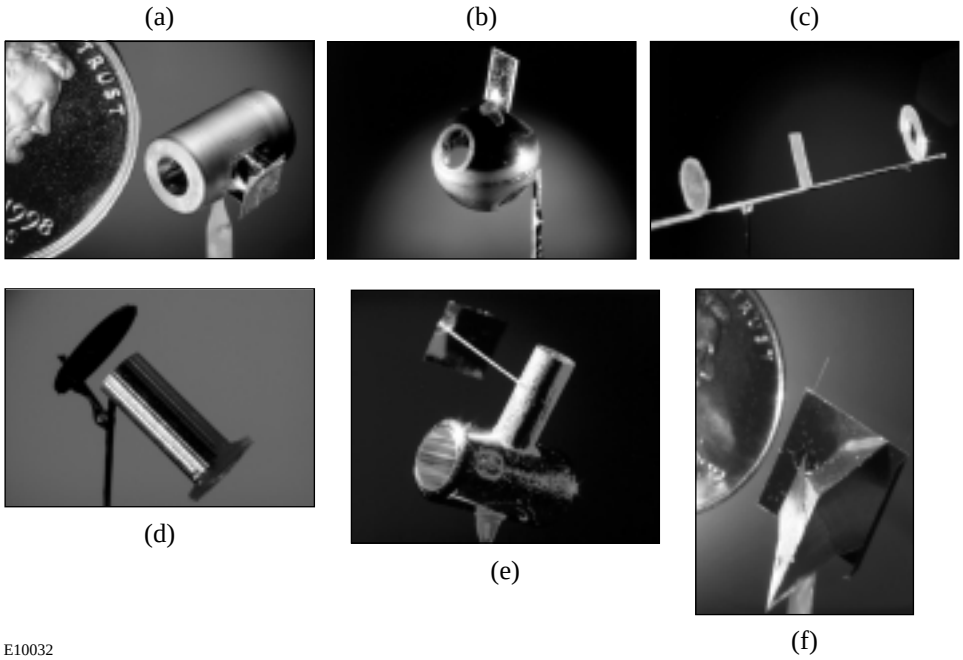

Figure 80.27
OMEGA routinely irradiates a variety of targets. (a) Cylindrical hohlraum target used for radiation ablation studies; (b) tetrahedral hohlraum target; (c) planar target; (d) direct-drive cylinder target; (e) radiation-driven shock target; and (f) x-ray diffraction target.

Table 80.VIII: Approved FY00 NLUF Proposals.

Principal Investigator	Affiliation	Proposal Title
R. Fisher	General Atomics	High-Spatial-Resolution Neutron Imaging of Inertial Fusion Target Plasmas Using Bubble Neutron Detectors
M. Myers	University of California at San Diego	Continuing Studies of Dynamic Properties of Shock-Compressed Solids by *In-Situ* Transient X-Ray Diffraction
R. P. Drake	University of Michigan	Supernova Hydrodynamics on the OMEGA Laser
R. Petrasso	Massachusetts Institute of Technology	Charged-Particle Spectroscopy on OMEGA: Recent Results, Next Steps
D. Cohen	Prism Computational Sciences	Development of X-Ray Tracer Diagnostics for Radiatively Driven NIF Ignition Capsule Ablators
K. Fletcher	SUNY Geneseo	Investigation of Solid-State Detection for Charged-Particle Spectroscopy
B. Afeyan	Polymath Research	Optical-Mixing-Controlled Stimulated Scattering Instability Experiments on OMEGA II: The Effects of Temporal Beam Smoothing and Crossing Angle Variation in CH and Al Plasmas.

Publications and Conference Presentations

Publications

S. R. Arrasmith, S. D. Jacobs, I. A. Kozhinova, L. L. Gregg, A. B. Shorey, H. J. Romanofsky, D. Golini, W. I. Kordonski, S. Hogan, and P. Dumas, "Studies of Material Removal in Magnetorheological Finishing (MRF) from Polishing Spots," in *Finishing of Advanced Ceramics and Glasses*, edited by R. Sabia, V. A. Greenhut, and C. G. Pantano, Ceramic Transactions, Vol. 102 (The American Ceramic Society, Westerville, OH, 1999), pp. 201–210.

A. Babushkin, W. A. Bittle, M. D. Skeldon, and W. Seka, "Diode-Pumped Regenerative Amplifier for the OMEGA Laser System," in *Conference on Lasers and Electro-Optics*, OSA Technical Digest (Optical Society of America, Washington, DC, 1999), pp. 407–408.

S.-H. Chen, J. C. Mastrangelo, and R. J. Jin, "Glassy Liquid Crystal Films as Broadband Polarizers and Reflectors via Spatially Modulated Photoracemization," Adv. Mater. **11**, 1183 (1999).

R. E. Giacone, C. J. McKinstrie, and T. Kolber, "Angular Dependence of Stimulated Brillouin Scattering in a Homogeneous Two-Dimensional Plasma," Phys. Plasmas **6**, 3587 (1999).

S. D. Jacobs, S. A. Arrasmith, I. A. Kozhinova, L. L. Gregg, A. B. Shorey, H. J. Romanofsky, D. Golini, W. I. Kordonski, P. Dumas, and S. Hogan, "An Overview of Magnetorheological Finishing (MRF) for Precision Optics," in *Finishing of Advanced Ceramics and Glasses*, edited by R. Sabia, V. A. Greenhut, and C. G. Pantano, Ceramic Transactions, Vol. 102 (The American Ceramic Society, Westerville, OH, 1999), pp. 185–199.

D. Katsis, P. H. M. Chen, J. C. Mastrangelo, S.-H. Chen, and T. N. Blanton, "Vitrified Chiral-Nematic Liquid Crystalline Films for Selective Reflection and Circular Polarization," Chem. Mater. **11**, 1590 (1999).

R. L. McCrory and J. M. Soures, "Status of Direct-Drive Inertial Confinement Fusion Research at the Laboratory for Laser Energetics," in *Current Trends in International Fusion Research*, edited by E. Panarella (NRC Research Press, Ottawa, Canada, 1999), pp. 251–259 (invited).

A. V. Okishev, D. Jacobs-Perkins, S. F. B. Morse, D. Scott, and W. Seka, "Prepulse Contrast Monitor for the OMEGA Driver Line," in *Conference on Lasers and Electro-Optics*, OSA Technical Digest (Optical Society of America, Washington, DC, 1999), pp. 406–407.

A. V. Okishev, "High-Repetition-Rate, Diode-Pumped, Multipass Preamplifier for the OMEGA Master Oscillator," in *Conference on Lasers and Electro-Optics*, OSA Technical Digest (Optical Society of America, Washington, DC, 1999), p. 407.

M. D. Skeldon, A. V. Okishev, R. L. Keck, and W. Seka, "An Optical Pulse-Shaping System Based on Aperture-Coupled Striplines for OMEGA Pulse-Shaping Applications," in *Conference on Lasers and Electro-Optics*, OSA Technical Digest (Optical Society of America, Washington, DC, 1999), p. 408.

V. A. Smalyuk, T. R. Boehly, D. K. Bradley, V. N. Goncharov, J. A. Delettrez, J. P. Knauer, D. D. Meyerhofer, D. Oron, D. Shvarts, Y. Srebro, and R. P. J. Town, "Nonlinear Evolution of Broad-Bandwidth, Laser-Imprinted Nonuniformities in Planar Targets Accelerated by 351-nm Laser Light," Phys. Plasmas **6**, 4022 (1999).

M. D. Wittman and R. S. Craxton, "Self-Interference Patterns and Their Application to Inertial-Fusion Target Characterization," Appl. Opt. **38**, 5365 (1999).

M. J. Zuerlein, D. Fried, J. D. B. Featherstone, and W. Seka, "Optical Properties of Dental Enamel in the Mid-IR Determined by Pulsed Photothermal Radiometry," IEEE J. Sel. Top. Quantum Electron. **5**, 1083 (1999).

Forthcoming Publications

R. Adam, M. Currie, C. Williams, R. Sobolewski, O. Harnack, and M. Darula, "Direct Observation of Subpicosecond Single-Flux-Quantum in Pulse-Driven Y-Ba-Cu-O Josephson Junctions," to be published in Applied Physics Letters.

R. Betti, "Radial Discontinuities in Tokamak MHD Equilibria with Poloidal Flow," to be published in Physics of Plasmas.

R. Betti and J. P. Freidberg, "Low-β, Magnetohydrodynamic Tokamak Equilibria with Poloidal Transonic Flow," to be published in Physical Review Letters.

T. R. Boehly, A. Babushkin, D. K. Bradley, R. S. Craxton, J. A. Delettrez, R. Epstein, T. J. Kessler, J. P. Knauer, R. L. McCrory, P. W. McKenty, D. D. Meyerhofer, S. P. Regan, W. Seka, S. Skupsky, V. A. Smalyuk, R. P. J. Town, and B. Yaakobi, "Laser-Uniformity and Hydrodynamic-Stability Experiments at the OMEGA Laser Facility," to be published in Laser and Particle Beams.

J. L. Chaloupka and D. D. Meyerhofer, "Observation of Electron Trapping in an Intense Laser Beam," to be published in Physical Review Letters.

J. L. Chaloupka and D. D. Meyerhofer, "Characterization of a Tunable Single-Beam Ponderomotive-Optical Trap," to be published in the Journal of the Optical Society of America B.

S.-H. Chen, J. C. Mastrangelo, B. M. Conger, and D. Katsis, "Design, Synthesis, and Potential Application of Glass-Forming Functional Organic Materials," to be published in the Proceedings of the 6th International Polymer Conference, Kusatsu, Japan, 20–24 October 1997 (invited).

S.-H. Chen, R. J. Jin, D. Katsis, J. C. Mastrangelo, S. Papernov, and A. W. Schmid, "Selective Reflection and Polarization Band of Glassy Chiral-Nematic Films Broadened by Photoracemization," to be published in Liquid Crystals.

M. Currie, C.-C. Wang, R. Sobolewski, and T. Y. Hsiang, "Picosecond Nodal Testing of Centimeter-Size Superconducting Nb Microstrip Interconnects," to be published in Applied Superconductivity.

F. Dahmani, J. C. Lambropoulos, A. W. Schmid, S. Papernov, and S. J. Burns, "Crack Arrest and Stress Dependence of Laser-Induced Surface Damage in Fused Silica and Borosilicate Glass," to be published in Applied Optics.

F. Dahmani, A. W. Schmid, J. C. Lambropoulos, and S. J. Burns, "Lifetime Prediction of Laser-Precracked Fused Silica Subjected to Subsequent Cyclic Laser Pulses," to be published in the Journal of Materials Science.

F.-Y. Fan, J. C. Mastrangelo, D. Katsis, and S.-H. Chen, "Novel Glass-Forming Liquid Crystals V. Nematic and Chiral-Nematic Systems with an Elevated Glass Transition Temperature," to be published in Liquid Crystals.

V. N. Goncharov, J. A. Delettrez, S. Skupsky, and R. P. J. Town, "Modeling Laser Imprint for Inertial Confinement Fusion Targets," to be published in Physical Review Letters.

K. Green and R. Sobolewski, "Extending the *S*-Parameter Approach to Linear Time-Varying Microwave Devices: Part I. Analysis," to be published in IEEE Microwave Theory and Techniques.

K. S. Il'in, M. Lindgren, M. Currie, S. I. Cherednichenko, A. D. Semenov, G. N. Gol'tsman, E. M. Gershenzon, and R. Sobolewski, "Picosecond Hot-Electron Energy Relaxation in NbN Superconducting Photodetectors," to be published in Applied Physics Letters.

S. D. Jacobs, S. A. Arrasmith, I. A. Kozhinova, L. L. Gregg, A. B. Shorey, H. J. Romanofsky, D. Golini, W. I. Kordonski, P. Dumas, and S. Hogan, "Magnetorheological Finishing: Computer Controlled Optics Manufacturing," to be published in the Bulletin of the American Ceramic Society.

J. P. Knauer, R. Betti, D. K. Bradley, T. R. Boehly, T. J. B. Collins, V. N. Goncharov, P. W. McKenty, D. D. Meyerhofer, V. A. Smalyuk, C. P. Verdon, S. G. Glendinning, D. H. Kalantar, and R. G. Watt, "Single-Mode Rayleigh–Taylor Growth-Rate Measurements with the OMEGA Laser System," to be published in Physics of Plasmas.

R. S. Knox, "Physical Aspects of the Greenhouse Effect and Global Warming," to be published in the American Journal of Physics.

M. Lindgren, W.-S. Zeng, M. Currie, R. Sobolewski, S. Cherednichenko, B. Voronov, and G. N. Gol'tsman, "Picosecond Response of a Superconducting Hot-Electron NbN Photodetector," to be published in Applied Superconductivity.

F. J. Marshall, "Direct-Drive, Hollow-Shell Implosion Studies on the 60-Beam, UV OMEGA Laser System," to be published in Physics of Plasmas.

C. J. McKinstrie and E. A. Startsev, "Forward and Backward Stimulated Brillouin Scattering of Crossed Laser Beams," to be published in Physical Review E.

A. B. Shorey, W. I. Kordonski, S. R. Gorodkin, S. D. Jacobs, R. F. Gans, K. M. Kwong, and C. H. Farney, "Design and Testing of a New Magnetorheometer," to be published in the Review of Scientific Instruments.

R. W. Short, "Stability of Self-Focused Filaments in Laser-Produced Plasmas," to be published in Physical Review Letters.

D. J. Smith, J. A. Warner, N. E. LeBarron, T. J. Kessler, S. LaDelia, J. P. Knauer, D. D. Meyerhofer, D. Oron, and D. Shvarts, "The Development of Ion-Etched Phase Plates," to be published in Applied Optics.

J. M. Soures, R. L. McCrory, R. Betti, W. Bittle, T. R. Boehly, R. Boni, D. K. Bradley, T. J. B. Collins, R. S. Craxton, J. A. Delettrez, W. R. Donaldson, R. Epstein, V. Glebov, V. N. Goncharov, D. R. Harding, P. A. Jaanimagi, R. L. Keck, J. H. Kelly, T. J. Kessler, J. P. Knauer, C. K. Li, S. J. Loucks, F. J. Marshall, P. W. McKenty, D. D. Meyerhofer, S. F. B. Morse, S. Padalino, R. Petrasso, P. B. Radha, S. Regan, W. Seka, R. W. Short, A. Simon, S. Skupsky, D. J. Smith, R. P. J. Town, B. Yaakobi, and J. D. Zuegel, "Recent Advances in Direct-Drive ICF Target Physics at the Laboratory for Laser Energetics," to be published in the Proceedings of the 1998 IAEA Conference, Yokohama, Japan, 19–24 October 1998.

Conference Presentations

The following presentations were made by R. P. J. Town at the 1999 Fusion Summer Study Workshop, Snowmass, CO, 11–23 July 1999: "The OMEGA Laser System," "Rayleigh–Taylor Experiments on the OMEGA Laser," and "Direct-Drive Issues on the NIF."

The following presentations were made at SPIE's International Symposium on Optical Science, Engineering, and Instrumentation, Denver, CO, 18–23 July 1999:

S. R. Arrasmith, I. A. Kozhinova, L. L. Gregg, H. J. Romanofsky, A. B. Shorey, S. D. Jacobs, D. Golini, W. I. Kordonski, P. Dumas, and S. Hogan, "Details of the Polishing Spot in Magnetorheological Finishing."

D. D. Meyerhofer, T. Ditmire, N. Hay, M. H. R. Hutchinson, M. B. Mason, and J. W. G. Tisch, "Measurements of the Spatio-Temporal Properties of High-Order Harmonics."

A. B. Shorey, L. L. Gregg, H. J. Romanofsky, S. R. Arrasmith, I. A. Kozhinova, and S. D. Jacobs, "A Study of Material Removal During Magnetorheological Finishing."

The following presentations were made at Inertial Fusion Sciences and Applications (IFSA) 1999, Bordeaux, France, 12–17 September 1999:

V. N. Goncharov, S. Skupsky, P. W. McKenty, J. A. Delettrez, R. P. J. Town, and C. Cherfiles-Clérouin, "Stability Analysis of Directly Driven OMEGA and NIF Capsules."

D. R. Harding, R. Q. Gram, M. D. Wittman, L. D. Lund, D. Lonobile, M. J. Shoup III, S. J. Loucks, G. Besenbruch, K. Schultz, A. Nobile, and S. Letzring, "Direct-Drive Cryogenic Targets and the OMEGA Cryogenic Target Handling System."

R. L. McCrory, R. E. Bahr, T. R. Boehly, T. J. B. Collins, R. S. Craxton, J. A. Delettrez, W. R. Donaldson, R. Epstein, V. N. Goncharov, R. Q. Gram, D. R. Harding, P. A. Jaanimagi, R. L. Keck, J. P. Knauer, S. J. Loucks, F. J. Marshall, P. W. McKenty, D. D. Meyerhofer, S. F. B. Morse, P. B. Radha, S. P. Regan, W. Seka, S. Skupsky, V. A. Smalyuk, J. M. Soures, C. Stoeckl, R. P. J. Town, M. D. Wittman, B. Yaakobi, J. D. Zuegel, R. D. Petrasso, D. G. Hicks, C. K. Li, and O. V. Gotchev, "OMEGA Experiments and Preparation for Direct-Drive Ignition on the National Ignition Facility."

D. D. Meyerhofer, T. R. Boehly, D. K. Bradley, T. J. B. Collins, J. A. Delettrez, Y. Fisher, V. N. Goncharov, O. Gotchev, J. P. Knauer, P. W. McKenty, S. P. Regan, W. Seka, S. Skupsky, V. A. Smalyuk, R. P. J. Town, and B. Yaakobi, "Direct-Drive Imprinting and Rayleigh–Taylor Experiments on OMEGA."

W. Seka, D. D. Meyerhofer, S. P. Regan, R. S. Craxton, B. Yaakobi, C. Stoeckl, A. Simon, R. W. Short, and R. E. Bahr, "NIF-Scale Direct-Drive Interaction on OMEGA."

S. Skupsky, T. J. B. Collins, R. S. Craxton, J. A. Delettrez, R. Epstein, V. N. Goncharov, P. W. McKenty, P. B. Radha, R. P. J. Town, D. D. Meyerhofer, W. Seka, and R. L. McCrory, "Simulation of OMEGA Experiments as a Prelude to Direct-Drive NIF Ignition Experiments."

B. Yaakobi, F. J. Marshall, V. Yu. Glebov, R. D. Petrasso, J. M. Soures, V. A. Smalyuk, D. D. Meyerhofer, W. Seka, J. A. Delettrez, and R. P. J. Town, "Spherical Implosion Experiments on OMEGA: Measurements of the Cold, Compressed Shell."

J. D. Zuegel, D. Jacobs-Perkins, J. Marozas, R. G. Roides, R. S. Craxton, J. H. Kelly, S. Skupsky, W. Seka, and S. Letzring, "Broadband Beam Smoothing on OMEGA with Two-Dimensional Smoothing by Spectral Dispersion."

S. R. Arrasmith, S. D. Jacobs, I. A. Kozhinova, A. B. Shorey, D. Golini, W. I. Kordonski, S. Hogan, and P. Dumas, "Development and Characterization of Magnetorheological Fluids for Optical Finishing," Fine Powder Processing '99, University Park, PA, 20–22 September 1999.

The following presentations were made at the Optical Society of America's Annual Meeting, Santa Clara, CA, 26 September–1 October 1999:

D. Golini and S. D. Jacobs, "Magnetorheological Finishing of Aspheres."

S. D. Jacobs, S. A. Arrasmith, I. A. Kozhinova, L. L. Gregg, H. J. Romanofsky, A. B. Shorey, D. Golini, W. I. Kordonski, P. Dumas, and S. Hogan, "Magnetorheological Finishing of KDP."

UNIVERSITY OF
ROCHESTER